SITE CHARACTERIZATION REPORT
SBAS: Baar (ZG) - Kantonsspital

Manuel Hobiger, Marco Pilz, Clotaire Michel, Jan Burjánek, Donat Fäh

Last Modification: 28th July, 2016

Schweizerischer Erdbebendienst (SED)
Service Sismologique Suisse
Servizio Sismico Svizzero
Servizi da Terratrembels Svizzer

ETH Zürich
Sonneggstrasse 5
8092 Zürich
Schweiz
manuel.hobiger@sed.ethz.ch

Contents

1 Summary

The new strong-motion station SBAS was constructed next to the Kantonsspital of the canton of Zug in Baar. We performed two passive seismic array measurements for the site characterization, both on a field next to the station site. The site characterization measurements showed that the fundamental frequency beneath the station is 1.1 Hz. There are no 2-dimensional site effects detected. Using different techniques (HRFK, WaveDec, SPAC), consistent dispersion curves can be determined for Love and Rayleigh waves. The Rayleigh wave ellipticity curve is complicated and shows at least two singular peaks and troughs. The joint inversions of all measured data indicate that there is a mode osculation in the Rayleigh waves around 4.3 Hz. The inversion resulted in a model consisting of three layers over the bedrock. The bedrock depth is around 100 m. The V_{S30} value is around 205 m/s.

2   Introduction

In the framework of the second phase of the Swiss Strong Motion Network (SSMNet) renewal project, a new station was planned in the canton of Zug. The site selection resulted in the identification of the Kantonsspital in Baar as the best location. The new station, called SBAS, was constructed on the western side of the hospital, next to an agricultural field. It went operational on 16 October 2014.

Figure 1: Map showing the location of station SBAS next to the Kantonsspital in Baar.
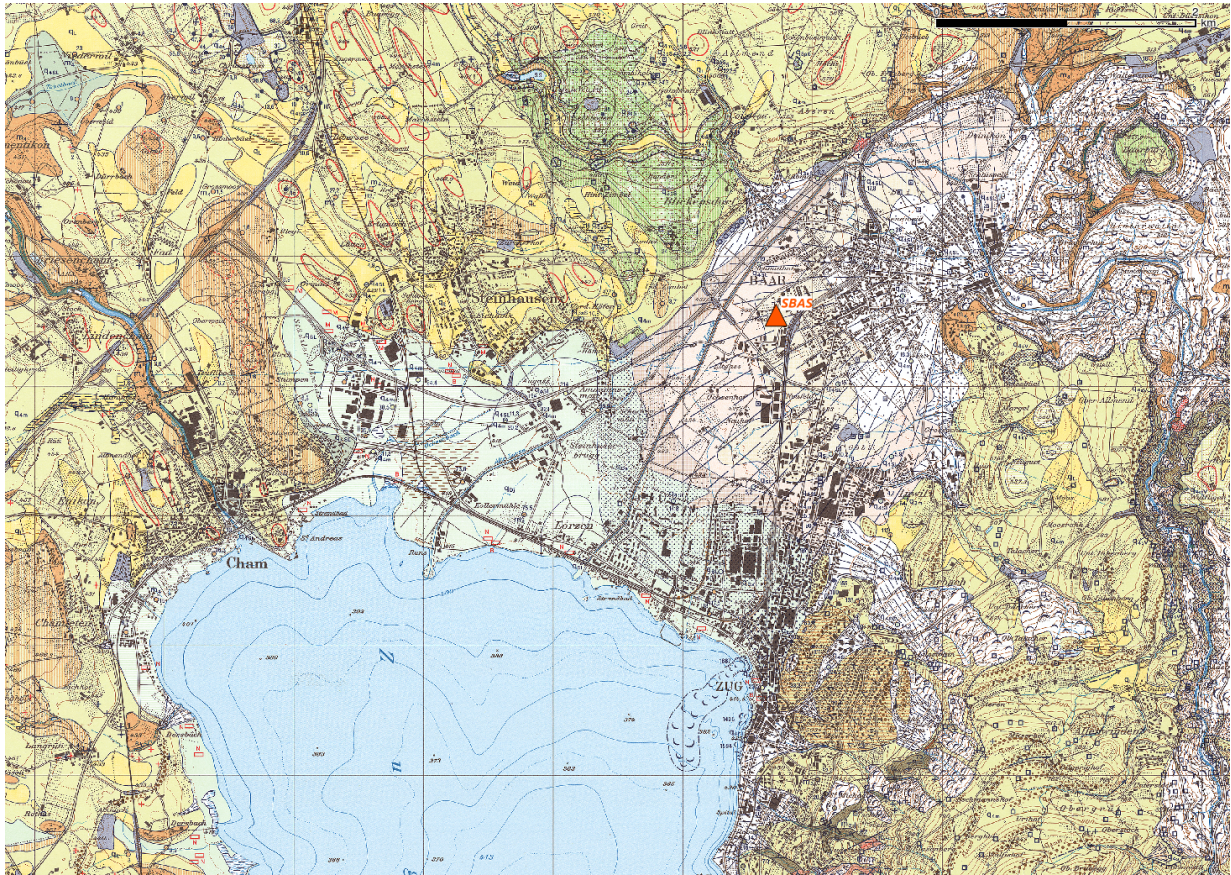
3 Geological setting

Figure 2: Geological map of the area north of Lake Zug. The geological atlas indicates changing layers of gravel, sand and silt for the underground of station SBAS.

The geological map of the northern part of Lake Zug (Fig. 2) shows the setting of station SBAS inside the alluvial cone of the Lorze river. The alluvial deposits consist of mixed layers of gravel, sand and silts. Due to the location in the alluvial basin, the groundwater level below the station is relatively high and may be found at a depth of around 1 m.

4 Site characterization

4.1 Measurements and data set

We investigated the local underground structure around station SBAS by passive seismic array measurements which took place on 2015 January 22, with a bit of snow lying on the ground. The earth was not completely frozen. The layout of the two seismic arrays is shown in Fig. 3. As the available space for an array measurement is limited by the hospital building to one side, we used the available space on the field to deploy the arrays.

Array 1 was installed first, it consisted of 14 stations in total. It was planned as consisting of a central station and three rings of three, five and five stations, respectively, with radii of 10, 25 and 50 m, respectively. The station names of this array are composed of "SBAS" followed by a two-digit number from 1 to 14.

In order to measure longer wavelengths and reach deeper layers, a second array was built by moving the stations from the 25-meter ring to other locations which were planned to lie on a ring with a radius of 100 m. However, in order to avoid the influence of the hospital building, the center of this second ring was moved around 40 m west of the center of the first array. All stations in the second array also have station names consisting of "SBAS" followed by a two-digit number, this time between 21 and 34, which were obtained by adding 20 to all station numbers of the first array.

The parameters of both arrays are given in Table 1.

The station locations have been measured by a differential GPS system (Leica Viva GS10) which was set up to measure with a precision better than 5 cm. Finally, the largest error of a station location was 2.2 cm.

Table 1: List of the seismic array measurements in Baar.

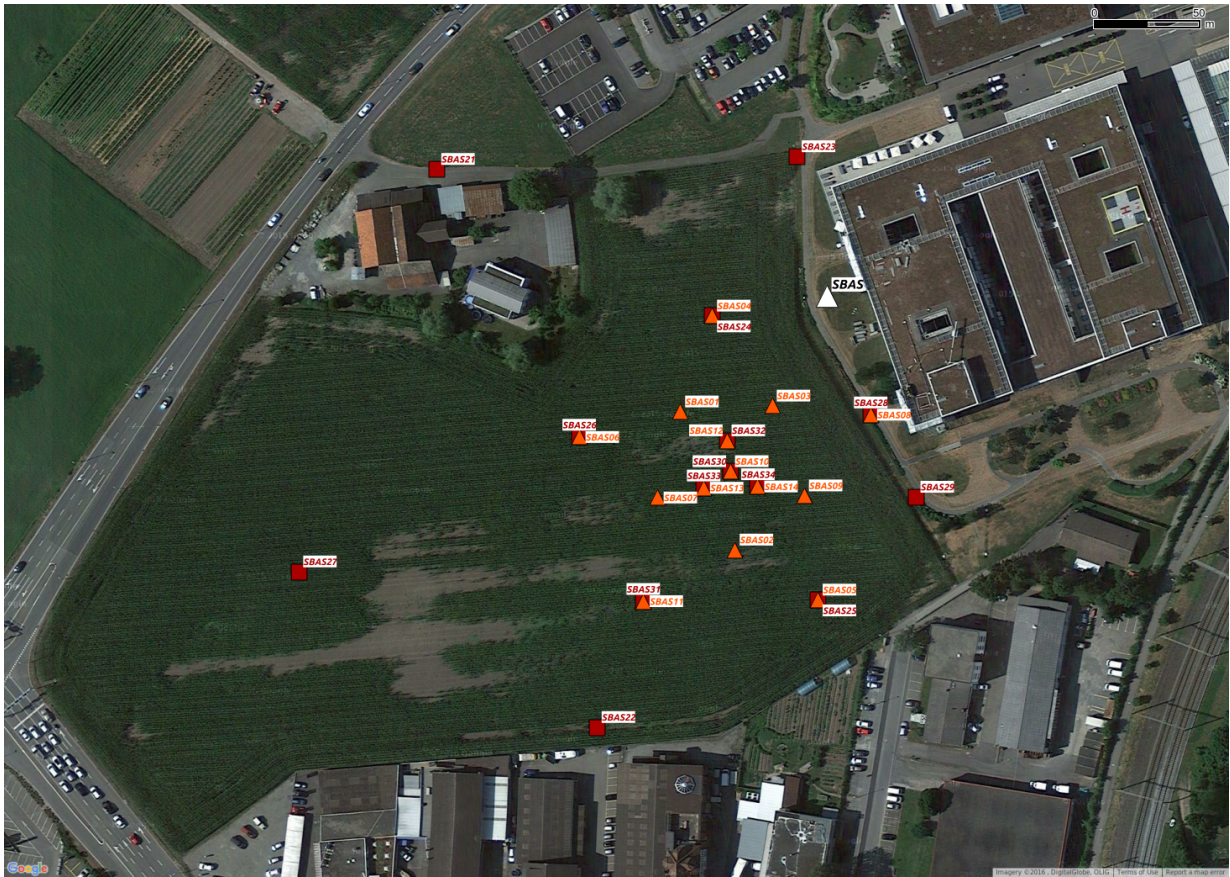| Array name	Number of sensors	Minimum interstation distance [m]	Maximum interstation distance [m]	Recording time [s]
1	14	10.0	97.0	5400
2	14	10.0	208.4	7800

Figure 3: Layout of the array measurements around station SBAS. The location of SBAS is indicated by the white triangle, the locations of the stations during the first array measurement by orange triangles and during the second array measurement by red squares.

4.2 Single-station measurement results

4.2.1 H/V curves

Figure 4 shows the H/V curves determined with the time-frequency analysis method (Fäh et al., 2009) for all stations of both arrays. The peak frequency of all stations is in very good agreement, all stations have a fundamental frequency of 1.1 Hz. There are some major differences between the different stations for frequencies above 1.5 Hz, but all curves are in qualitative agreement and show a secondary peak at frequencies between 3.5 and 4.0 Hz. In the larger array, there is more scatter in the curves because the outer stations differ more from the central ones.
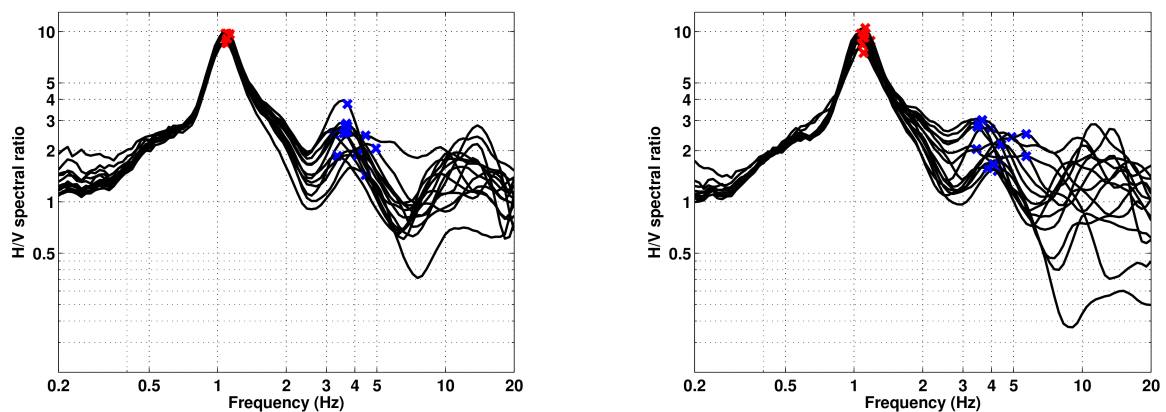

Figure 4: Overview of the H/V measurements for the different stations of first array measurement (left) and the second array measurement (right).

4.2.2 RayDec ellipticity curves

The RayDec technique (Hobiger et al., 2009) is meant to eliminate the contributions of other wave types than Rayleigh waves and give a better estimate of the ellipticity than the classical H/V technique. The RayDec ellipticity curves for all stations of the array measurements are shown in Fig. 5.

Here again, the curves for the different stations in the small array are in very good agreement with each other below 2 Hz. The ellipticity peak is clear at 1.1 Hz. There is more scattering at higher frequencies, but all stations show a clear secondary peak around 4 Hz as well as a secondary trough around 6 Hz. The curves for the large array are similar, but some stations show slightly higher ellipticities during this later measurement. The ellipticities for station SBAS10/SBAS30, the central station of the arrays, and station SBAS04/SBAS24, the station closest to the permanent station SBAS, are similar around the fundamental peak, but differ for higher frequencies.
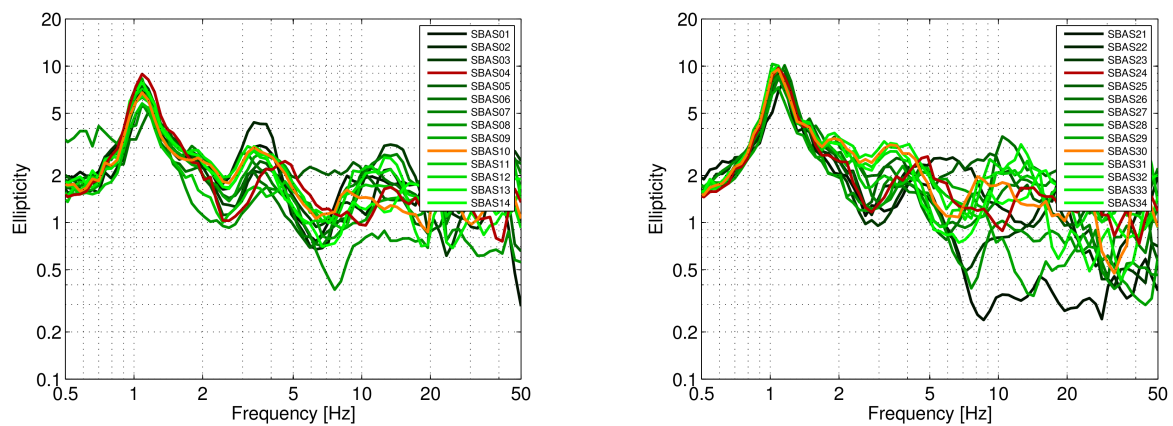

Figure 5: RayDec ellipticities for array 1 (left) and array 2 (right).

4.2.3 Polarization measurements

The polarization parameters of the seismic noise recordings of all stations of the two arrays are similar and do not show significantly polarized particle motions. As an example, the polarization analysis results for stations SBAS10 and SBAS30 are shown in Fig. 6. This is the central station of the array, which measured both in the small array (SBAS10) and in the large array (SBAS30). The analysis was performed according to Burjánek et al. (2010) and Burjánek et al. (2012).

The polarization results of SBAS10 and SBAS30 are very similar. This means that the properties of the noise wave field did not change significantly between the measurements in the small and large arrays. The particle motion is mostly linearly polarized around 1 Hz and also around 4 Hz, i.e. at the resonance frequencies that where already seen in the H/V curves. At lower and higher frequencies, the particle motion is not polarized. There are no preferred strike directions, i.e. there is no 2- or 3-dimensional wave propagation effect in the valley.
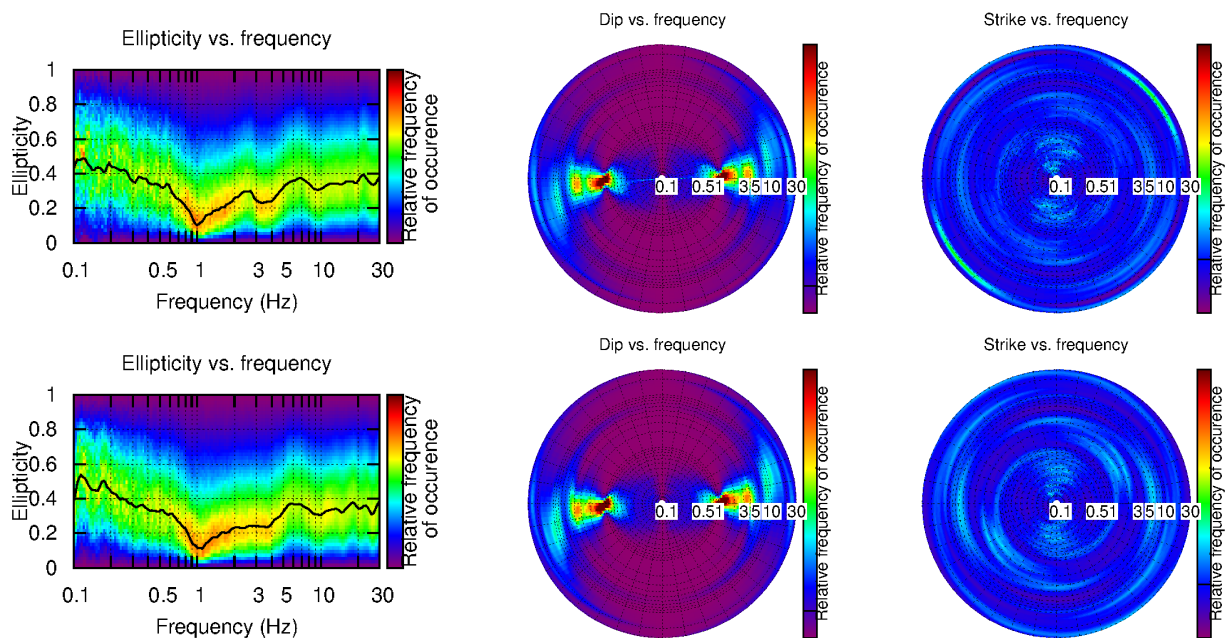

Figure 6: Polarization analysis of stations SBAS10 and SBAS30 (from top to bottom).

4.3   3-component high-resolution FK

The results of the 3-component high-resolution FK analysis (Poggi and Fäh, 2010) of both arrays are shown in Figs 7 and 8. On the vertical component, a continuous dispersion curve is clearly visible in both arrays, but only up to around 8 Hz. The theoretical upper resolution limit cannot be reached. On the radial component, a similar dispersion curve can be retrieved in the same frequency ranges, but there is a gap around 6 Hz where the curve is not visible. At higher frequencies, it becomes visible again. The higher frequency part is compatible with the vertical dispersion curve in the same frequency range, but it is unclear if both parts of the dispersion curve belong to the same mode or to different modes.

On the transverse component, the fundamental Love wave dispersion curve is well identified in both arrays, but also here the high-frequency theoretical array resolution limit cannot be reached.

In all cases, the curves of both arrays are in very good agreement and no additional modes can be identified.

The ellipticity curves determined with the 3-component HRFK analysis are shown in Fig. 8.
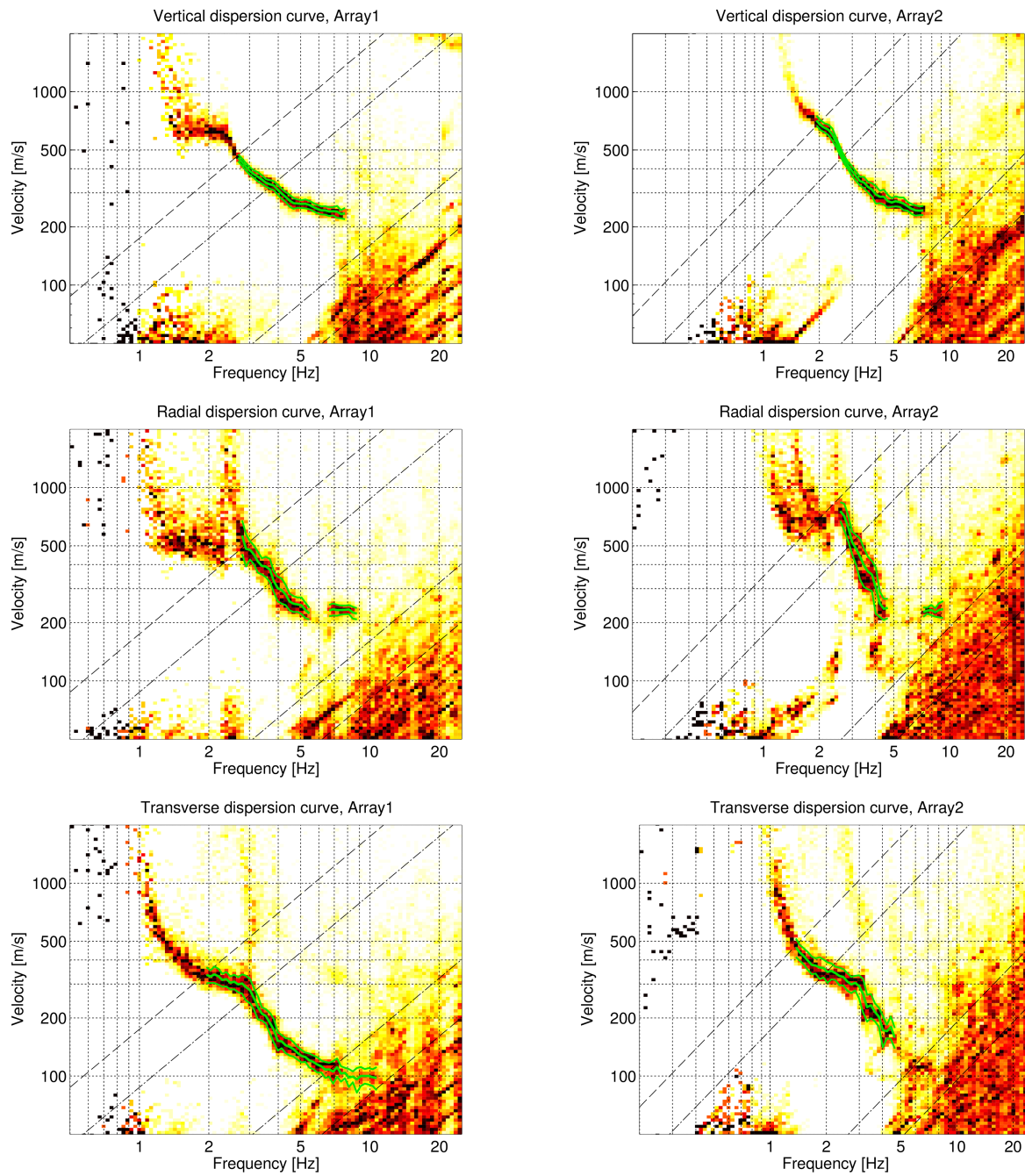
Figure 7: Dispersion curves obtained with the 3-component HRFK algorithm (Poggi and Fäh, 2010). In the left column, the results for array 1 are shown, in the right column for array 2. The lines from top to bottom show the results for the vertical, radial and transverse components, respectively. The dashed and dotted black lines are the array resolution limits. The solid green lines are picked from the data, where the central line indicates the best values and the two outer lines the standard deviation.
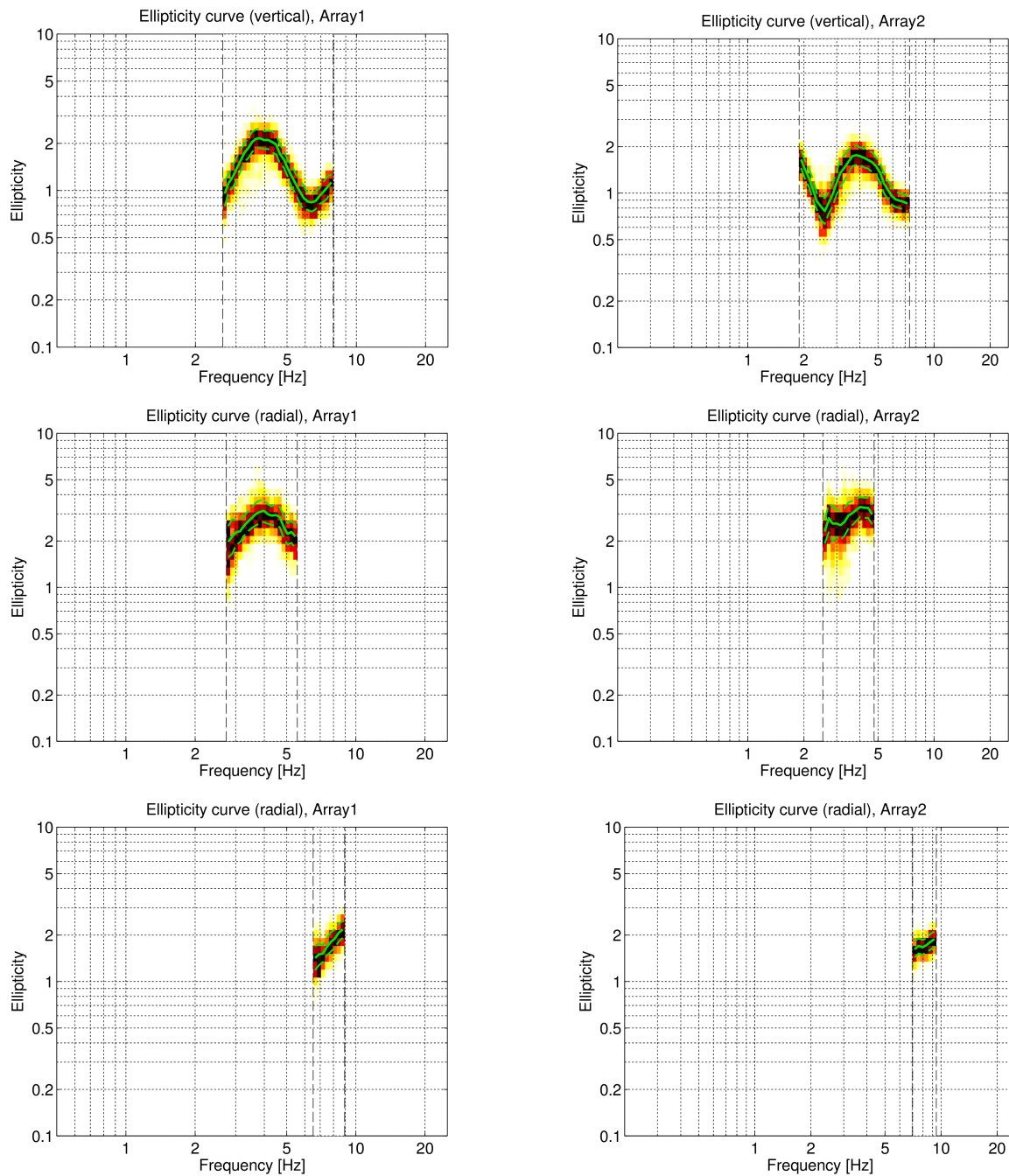
13

Figure 8: Ellipticity curves obtained with the 3-component HRFK algorithm (Poggi and Fäh, 2010) for array 1 (left) and array 2 (right). The frequency ranges of the different curves correspond to the ranges where the dispersion curves had been picked. Top: Results for the vertical component. Center: Results for the first mode of the radial component. Bottom: Results for the second mode of the radial component.

4.4 WaveDec

The results of the WaveDec (Maranò et al., 2012) processing are shown in Figs 9 - 12. This technique estimates the properties of single or multiple waves simultaneously with a maximum likelihood approach. We applied it once estimating only the properties of a single Love wave (modeling L), once estimating the properties of a single Rayleigh wave (modeling R) and once estimating one Love and one Rayleigh wave in the same time (modeling LR), both for arrays 1 and 2.

As can be seen in Fig. 9, the Love waves are clearly retrieved in both arrays and are in good agreement. The Rayleigh wave dispersion curve (Fig. 10) is also well retrieved in all cases, but here again the theoretical array resolution limits are not reached. Overall, there are no major differences between the L and LR modelings and the R and LR modelings, respectively.

The ellipticity curves in Figs 11 and 12 are plotted in two ways. On the left side, the ellipticity angle is shown. On the right side, the ellipticity is shown. The WaveDec code actually estimates the ellipticity angle. Ellipticity is the tangent of this angle. A negative ellipticity angle stands for retrograde particle motion, a positive ellipticity angle for prograde particle motion.

For array 1 and both the R and the LR modeling, the ellipticity is retrograde up to about 3.5 Hz, then switches to prograde until around 6 Hz and becomes retrograde above that frequency again. In the ellipticity this corresponds to a singular ellipticity peak at 3.5 Hz and a trough at 6 Hz.

With array 2, lower frequencies can be resolved. We see in the LR modeling that there is another change to prograde particle motion below 2.5 Hz, corresponding to another ellipticity trough at that frequency. The fundamental ellipticity peak at 1.1 Hz, which was resolved by the H/V and RayDec techniques, cannot be resolved with the array techniques.
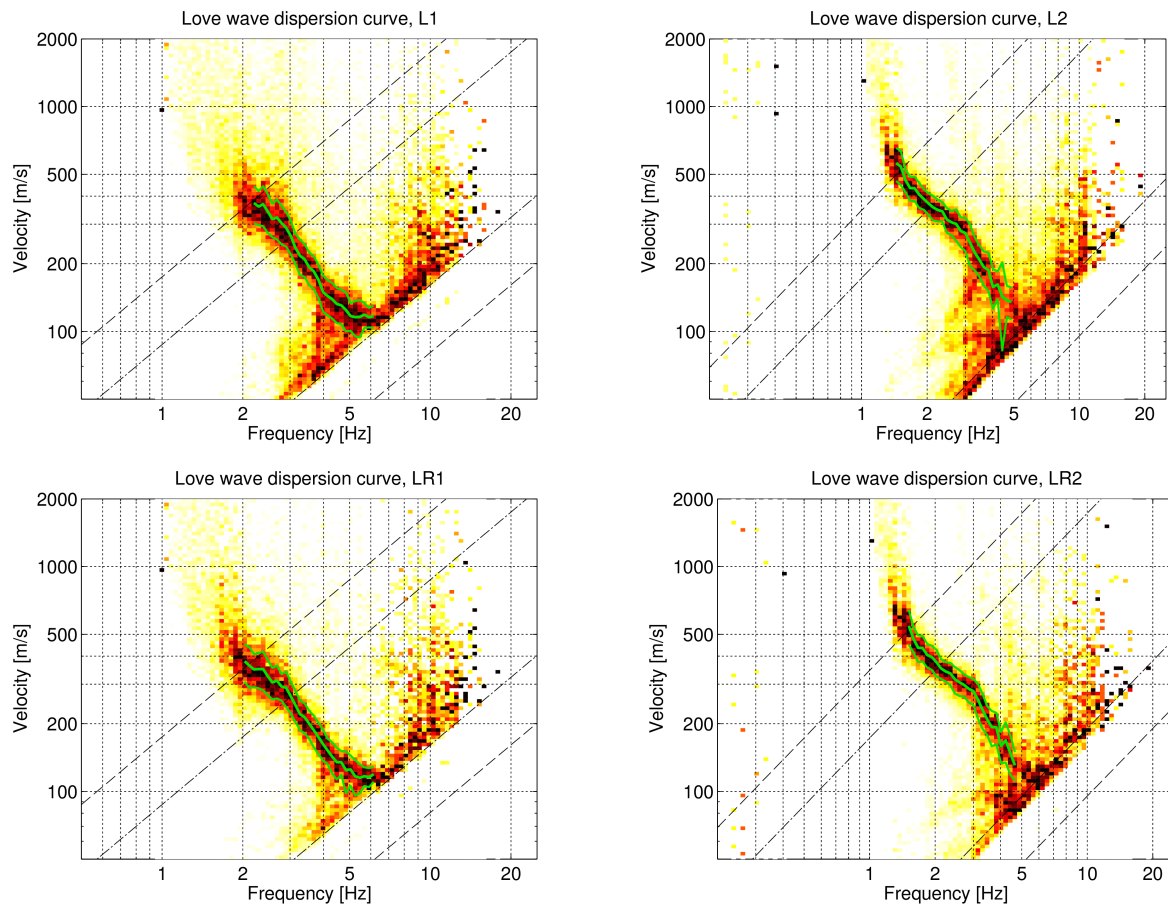
Figure 9: Love wave dispersion curves obtained with the WaveDec technique (Maranò et al., 2012). The first line shows the results for the analysis of only Love waves, the second line for estimating the Love and Rayleigh wave contributions simultaneously. The left plots correspond to array 1, the right ones to array 2. The dashed lines indicate the theoretical array resolution limits.
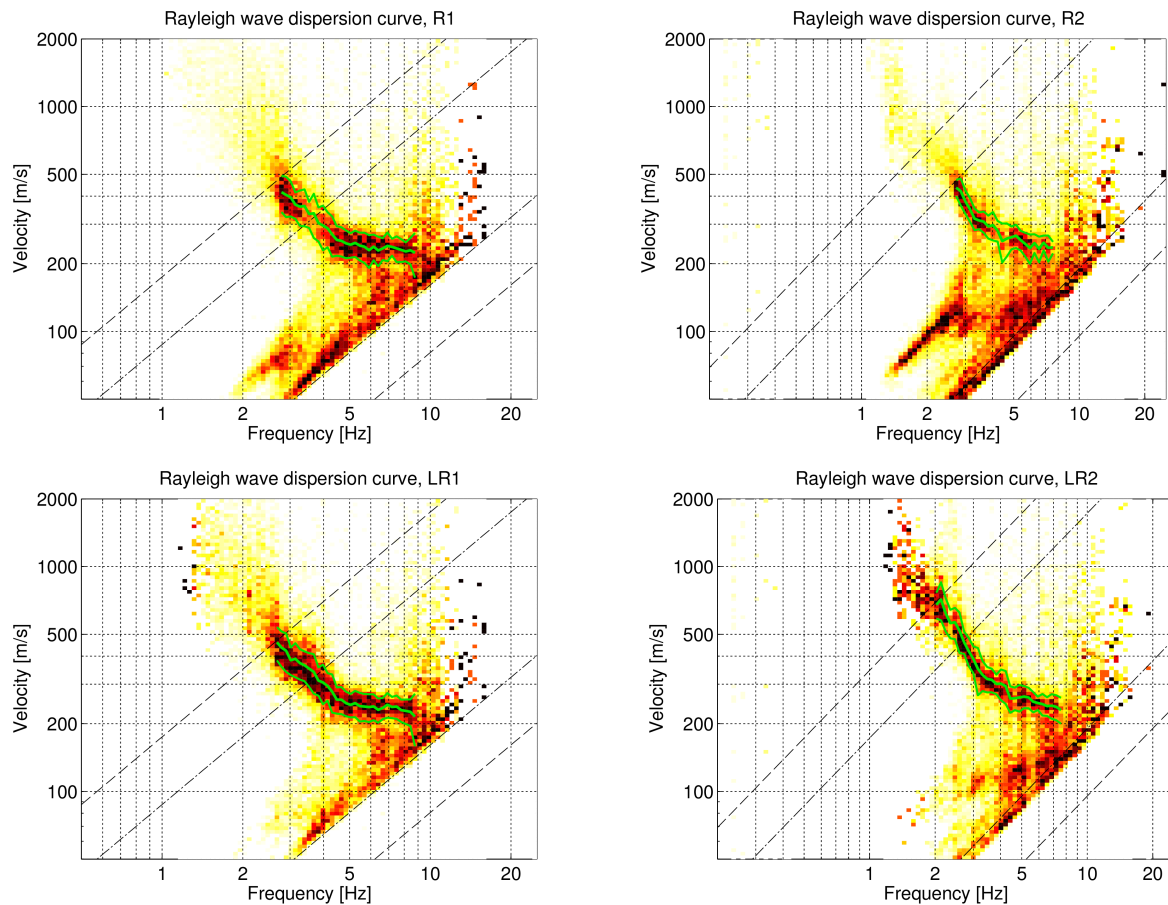
Figure 10: Rayleigh wave dispersion curves obtained with the WaveDec technique (Maranò et al., 2012). The first line shows the results for the analysis of only Rayleigh waves, the second line for estimating the Love and Rayleigh wave contributions simultaneously. The left plots correspond to array 1, the right ones to array 2. The dashed lines indicate the theoretical array resolution limits.
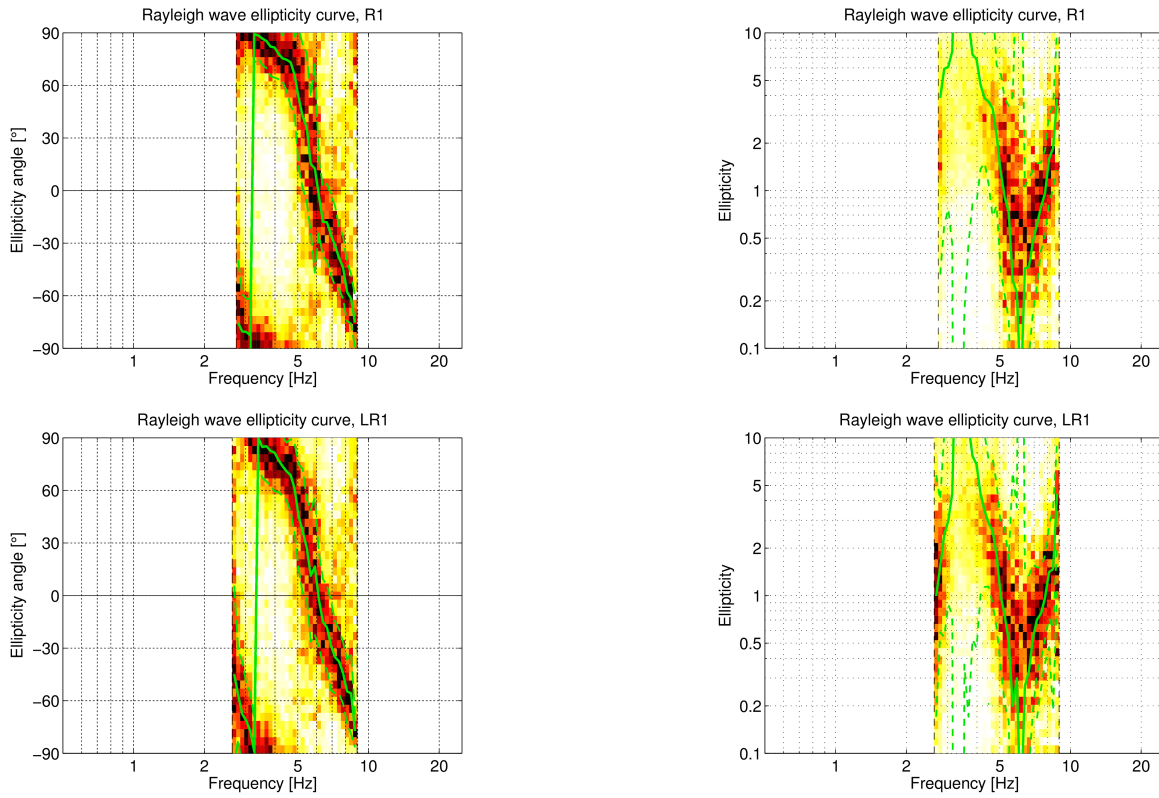
Figure 11: Rayleigh wave ellipticity curves obtained with the WaveDec technique (Maranò et al., 2012) for array 1. The left column shows the ellipticity angles, the right column the tangent of this angle, i.e. the ellipticity. The different rows show the R and LR analyses.
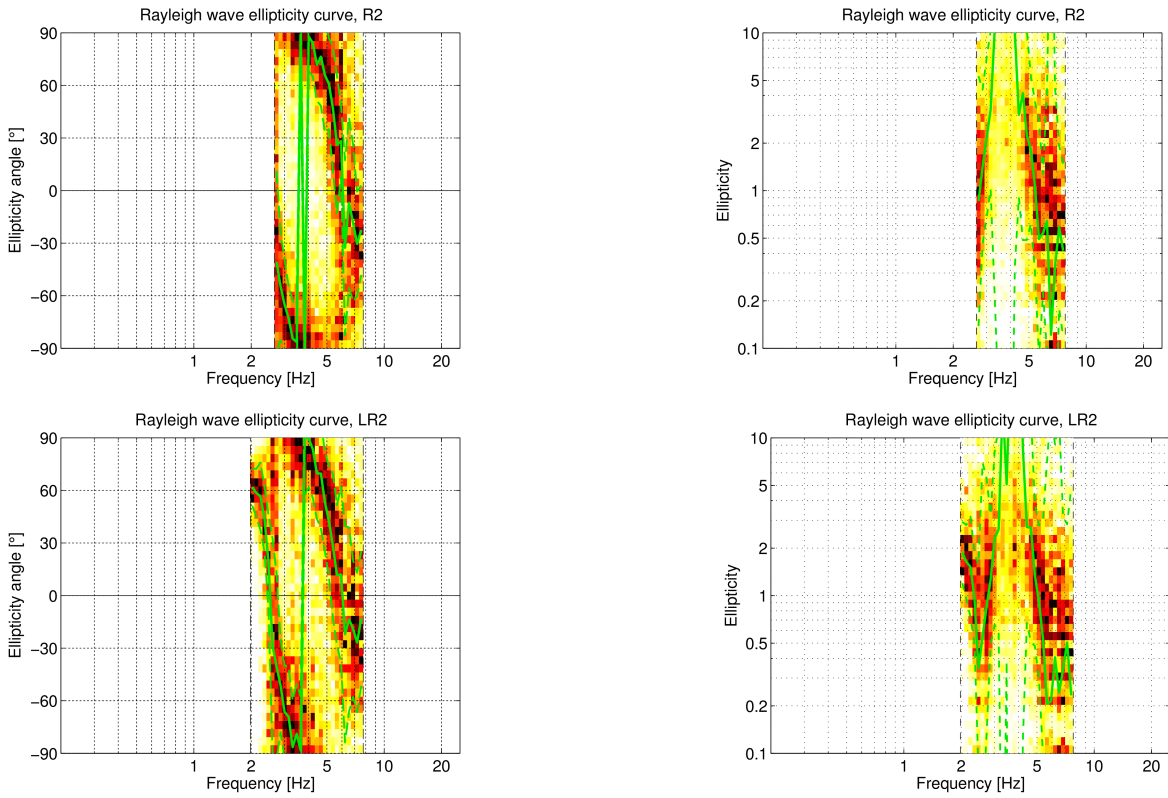
Figure 12: Rayleigh wave ellipticity curves obtained with the WaveDec technique (Maranò et al., 2012) for array 2. The left column shows the ellipticity angles, the right column the tangent of this angle, i.e. the ellipticity. The first and second rows show the results for the fundamental mode, the third and fourth rows for the first harmonic mode of the R and LR analyses, respectively.

4.5 SPAC

For both arrays, we also calculated the SPAC (Aki, 1957) curves of the vertical components, using the M-SPAC (Bettig et al., 2001) technique implemented in geopsy. In order to do so, rings with different radius ranges have been defined. For all station pairs with distance inside this radius range, the cross-correlation is calculated in different frequency ranges. These cross-correlation curves are averaged for all station pairs of the respective ring and give the SPAC curve. The rings are defined in such a way that at least three station pairs contribute and that their connecting vectors have a good directional coverage.

The SPAC curves for all defined rings are shown in Figs 13 and 14, respectively. The black points indicate the data values which contributed to the final dispersion curve estimation, which was made with the function `spac2disp` of the geopsy package. These resulting dispersion curves are shown in Fig. 15. For array 1, the dispersion curve is retrieved between 1.4 and 7.0 Hz. For array 2, it is retrieved between 1.3 and 6.8 Hz.
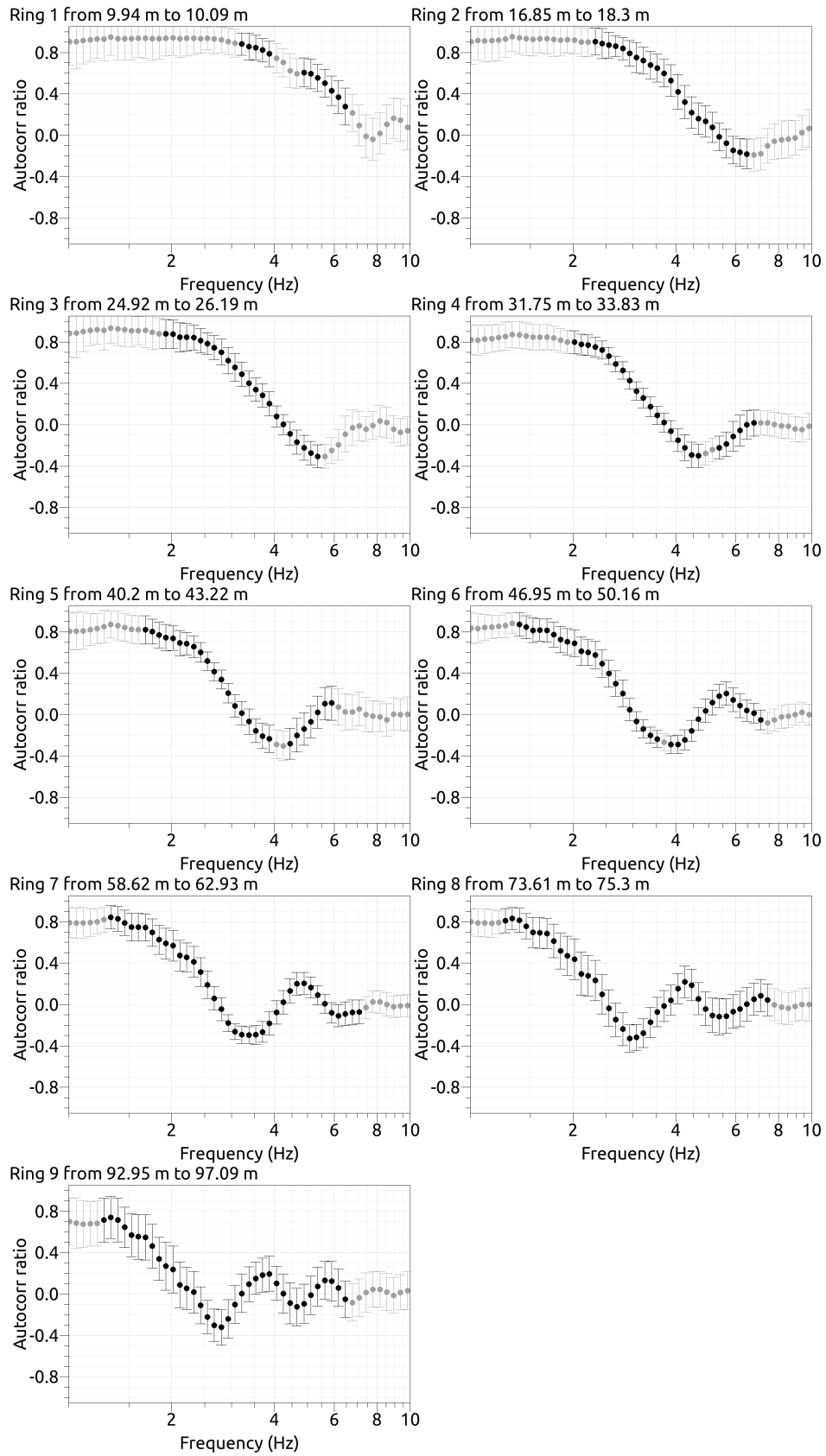
Figure 13: SPAC curves for array 1. The black data points contributed to the dispersion curve estimation.
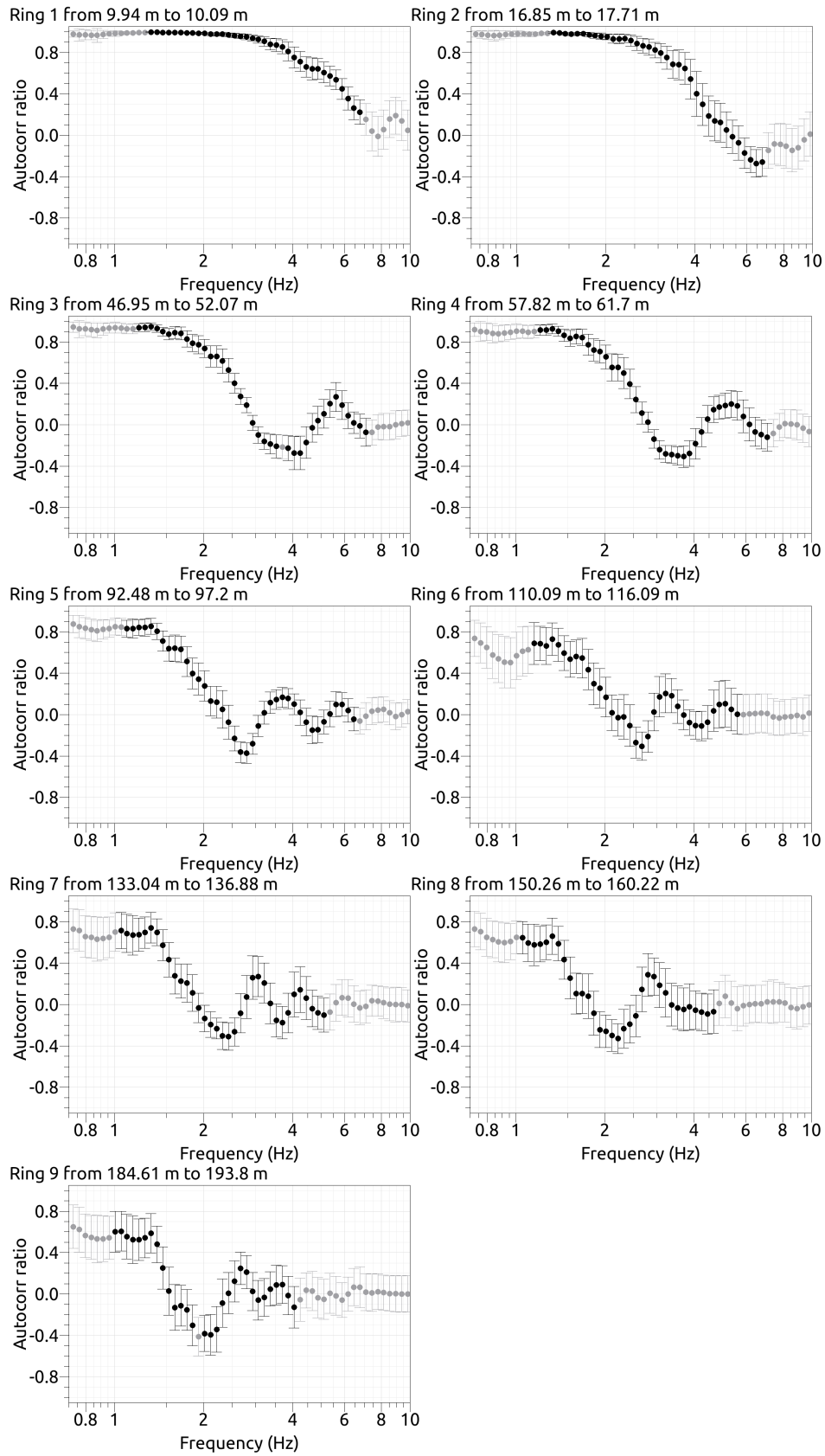
Figure 14: SPAC curves for array 2. The black data points contributed to the dispersion curve estimation.
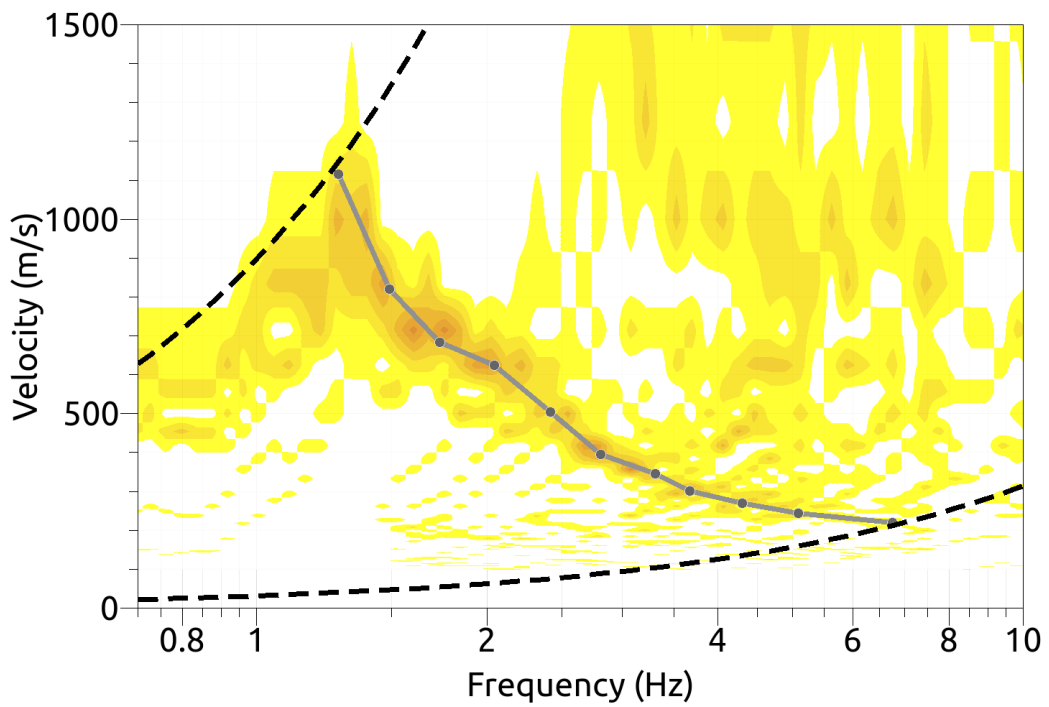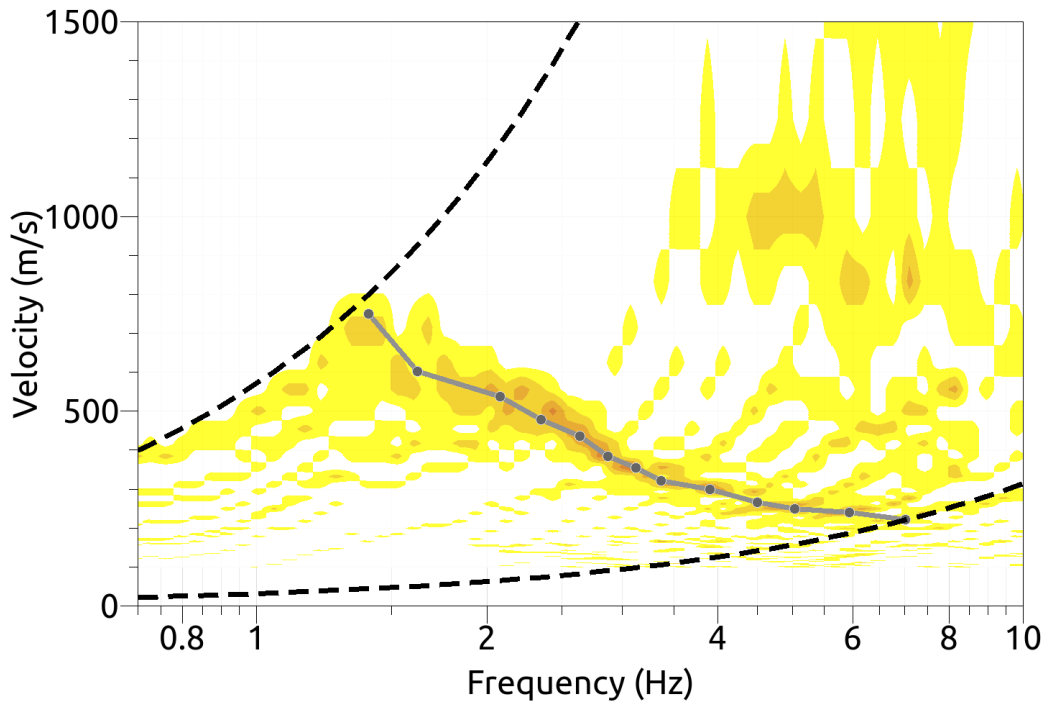
Figure 15: Resulting Rayleigh wave velocities for array 1 (top) and array2 (bottom). The gray line corresponds to the picked dispersion curve. The black curves are resolution limits, which are different from the FK analysis resolution limits.

4.6 Summary

Fig. 16 gives an overview of the dispersion and ellipticity curves determined by the different methods. The Love wave dispersion curves for the different methods in both arrays are in good agreement. Only below 2 Hz, the high-resolution FK and WaveDec curves differ significantly.

For the Rayleigh waves, the different methods differ more. The HRFK results of the vertical component are in very good agreement with the WaveDec results, but the radial component differs below 4 Hz, giving higher velocities. SPAC yields curves to lower frequencies than the FK resolution limits, but the velocities seem lower than for the other methods. The Rayleigh wave dispersion curve seems to consist of only one mode, but a small doubt remains from the radial results of HRFK, as there could also be an osculation of the fundamental and the first harmonic Rayleigh wave modes around 4.3 Hz.

The ellipticity curves for the different methods differ, but are in good qualitative agreement. RayDec gives an ellipticity curve at a wide frequency range, but the measurement in the afternoon (SBAS30) gives a higher ellipticity than in the morning (SBAS10). This might be caused by a higher part of Love waves in the wave field in the afternoon (the traffic on the surrounding streets was stronger). Therefore, the SBAS10 curve should be more reliable. The HRFK ellipticity curves are lower than the RayDec curves in their respective frequency ranges, but the trough and peak frequencies agree. With WaveDec (best result with LR2), there are three clear changes in the particle motion from prograde to retrograde and vice versa visible. The frequencies of these changes correspond well with the peak and trough frequencies of the RayDec and HRFK curves, even if the latter methods cannot resolve the absolute values of the ellipticity around the singularities due to methodological problems. In any case, the RayDec information for the fundamental peak can be nicely linked together with the WaveDec results at higher frequencies to form a single ellipticity curve. This curve corresponds to the fundamental Rayleigh wave mode.
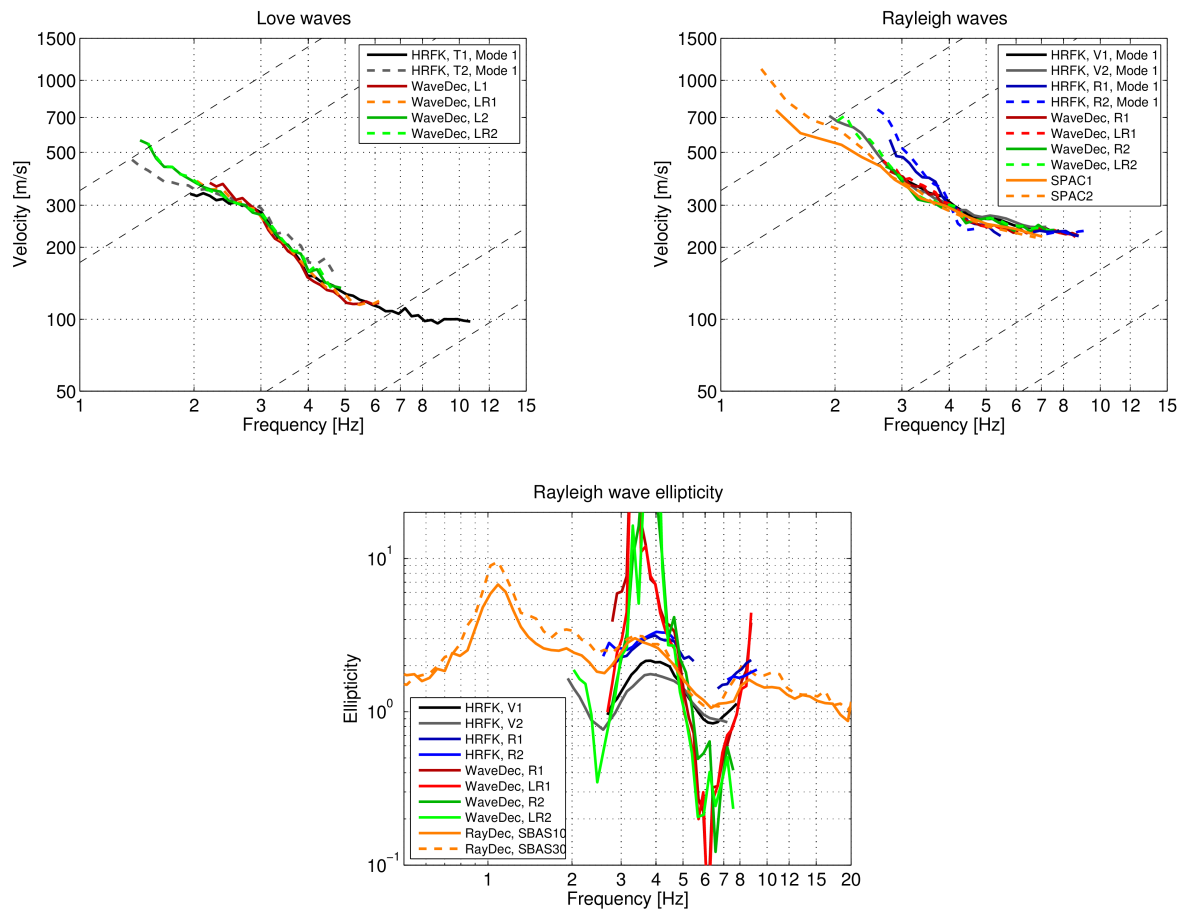
Figure 16: Overview of the Love and Rayleigh wave dispersion curves as well as the ellipticity curves for both arrays. The dashed lines indicate the theoretical resolution limits of the respective arrays (the upper frequency limits corresponds to array 1, the lower one to array 2). The RayDec ellipticity curves correspond to station SBAS10/SBAS30.

5 Data inversion

5.1 Inversion data

As all measurements fit together, it is not difficult to define the targets for the inversion. For the fundamental Rayleigh wave dispersion curve, the vertical HRFK curve of array 2 is used. Array 1 does not add valuable information at higher frequencies in that case and is therefore not included. For the Love wave dispersion curve, the transverse HRFK curve for array 1 is used at high frequencies and the WaveDec LR2 curve at lower frequencies. The ellipticity curve is combined from different techniques, using RayDec for the left and right flank of the fundamental peak, WaveDec LR2 for the first trough and the second peak and finally LR1 for the second trough.

In a first inversion run, all data curves are interpreted as the fundamental modes of Rayleigh and Love waves, respectively. A second inversion takes a possible osculation in the Rayleigh wave dispersion curves into account and interprets the Rayleigh waves above 4.3 Hz as the first harmonic mode.

The data curves that have been used for the inversion are indicated in Tables 2 and 3 and are shown in Fig. 17.
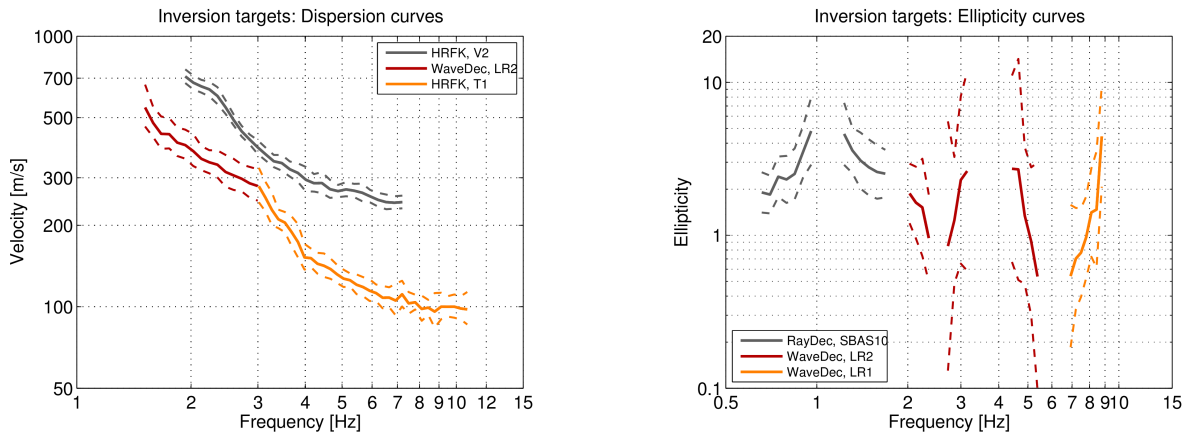

Figure 17: Overview of the dispersion and ellipticity curves used as targets for the different inversions.

Table 2: List of the data curves used as targets in the inversions without a possible mode osculation.

Array	Method	Wave type	Mode	Curve type	Frequency range [Hz]
1	HRFK (V)	Rayleigh	fundamental	dispersion	1.97 - 7.04
2	WaveDec LR2	Love	fundamental	dispersion	1.55 - 2.98
1	HRFK (T)	Love	fundamental	dispersion	3.00 - 10.63
1	RayDec (SBAS10)	Rayleigh	fundamental	ellipticity	0.65 - 0.93
1	RayDec (SBAS10)	Rayleigh	fundamental	ellipticity	1.26 - 1.67
2	WaveDec LR2	Rayleigh	fundamental	ellipticity	2.04 - 2.35
2	WaveDec LR2	Rayleigh	fundamental	ellipticity	2.78 - 3.09
2	WaveDec LR2	Rayleigh	fundamental	ellipticity	4.50 - 5.36
1	WaveDec LR1	Rayleigh	fundamental	ellipticity	7.04 - 8.66

Table 3: List of the data curves used as targets in the inversions including a possible mode osculation.

Array	Method	Wave type	Mode	Curve type	Frequency range [Hz]
1	HRFK (V)	Rayleigh	fundamental	dispersion	1.97 - 4.07
1	HRFK (V)	Rayleigh	harmonic	dispersion	4.35 - 7.04
2	WaveDec LR2	Love	fundamental	dispersion	1.55 - 2.98
1	HRFK (T)	Love	fundamental	dispersion	3.00 - 10.63
1	RayDec (SBAS10)	Rayleigh	fundamental	ellipticity	0.65 - 0.93
1	RayDec (SBAS10)	Rayleigh	fundamental	ellipticity	1.26 - 1.67
2	WaveDec LR2	Rayleigh	fundamental	ellipticity	2.04 - 2.35
2	WaveDec LR2	Rayleigh	fundamental	ellipticity	2.78 - 3.09
2	WaveDec LR2	Rayleigh	harmonic	ellipticity	4.50 - 5.36
1	WaveDec LR1	Rayleigh	harmonic	ellipticity	7.04 - 8.66

5.1.1 Inversion parameterization

From the geological information, we only know that the underground profile should consist of layers of gravel, sand and silt. However, the ellipticity curve shows various singularities with at least two peaks and two troughs. Such a complex ellipticity curve indicates that the underground structure is not that simple. Therefore, we expect a more complex structure of the underground. Therefore, underground models with different complexities were used as inversion parameterizations, ranging from three to eight layers (including the bedrock). In the inversions without possible osculation, the first layer's depth was allowed to range from 1 to 20 m, the depths of the other layers were limited to the range from 5 to 100 m. For the deepest two or three layers, the depths could range to 200 m. In the inversions with possible osculation, the first two layers could have depths from 1 to 20 m, all the other depth ranges were similar. The shear-wave velocity of the top layer ranged from 50 to 300 m/s (v_P from 80 to 1 000 m/s), the one of the second layer from 100 to 1 000 m/s (v_P from 100 to 2 000 m/s) and for all other layers from 150 to 3 500 m/s (v_P from 200 to 5 000 m/s). The density was fixed to 2 300 kg/m^3 for the lowest layer and to 2 000 kg/m^3 for all other layers.

5.2 Inversion results

We performed a total of twelve inversions with different parameterizations (see Table 4). Each inversion run produced 200 000 total models in order to assure a good convergence of the solution. The results of the inversions without possible osculation are shown in Figs 18 - 23, for the inversion with osculation in Figs 24 - 29.

Except for the three-layer inversions, all inversions of the respective inversion families yielded very similar minimum misfit values. This indicated that they all fitted the data equally well, but the best models may well differ. The three-layer model has a significantly larger misfit than the other models. This comes partly from the worse fit of the Love wave dispersion curve, but mainly from the bad fit of the ellipticity curve with its many peaks and troughs. A three-layer model can obviously produce such a complex ellipticity function with two peaks and two troughs, but it does not fit well in the present case.

In the runs without osculation, the Love wave dispersion curve is well fitted. The Rayleigh wave dispersion curve is also well fitted, but the part of the curve above 6 Hz is badly fitted. The fundamental peak of the ellipticity curve is remarkably fitted, as well as the first trough and the second peak. However, in the area of the right flank of the second peak and around the second trough, there are major differences in all cases.

In the runs including osculation, the fit of the Love wave dispersion curve is similar to the other cases. The fit of the fundamental Rayleigh wave dispersion curve is remarkable in all inversion runs, also the part identified as first harmonic mode is very well fitted. The parts of the ellipticity curve now attributed to the first harmonic mode are also better fitted than in the previous inversions. As the data are better fitted in the cases with osculation, the minimum misfit values of these inversions are also systematically smaller than for the previous inversions. Therefore, these inversions are the preferred inversions. All inversions between four and eight layers can be accepted as reasonable solutions.

Table 4: List of inversions

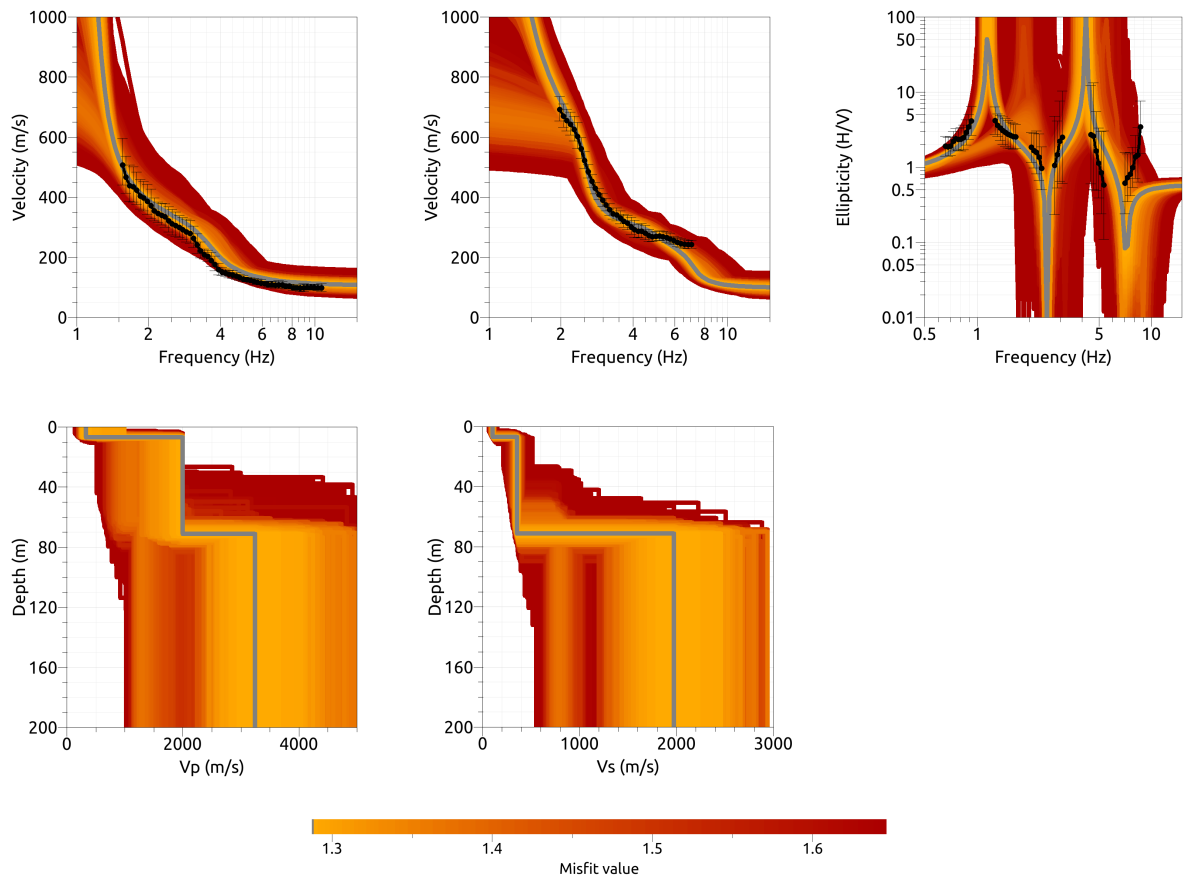| Inversion	Number of layers	Number of models	Minimum misfit
SBAS03	3	200 000	1.289
SBAS04	4	200 000	0.784
SBAS05	5	200 000	0.791
SBAS06	6	200 000	0.799
SBAS07	7	200 000	0.789
SBAS08	8	200 000	0.773
SBAS03osc	3	200 000	0.865
SBAS04osc	4	200 000	0.418
SBAS05osc	5	200 000	0.494
SBAS06osc	6	200 000	0.495
SBAS07osc	7	200 000	0.542
SBAS08osc	8	200 000	0.551

Figure 18: Inversion SBAS03: Love wave fundamental mode dispersion curve (top left), Rayleigh wave fundamental mode dispersion curve (top center), Rayleigh wave ellipticity curve (top right), P-wave velocity profiles (center left) and S-wave velocity profiles (center right). The black dots indicate the data points used for the inversion, the gray line indicates the best-fitting model.
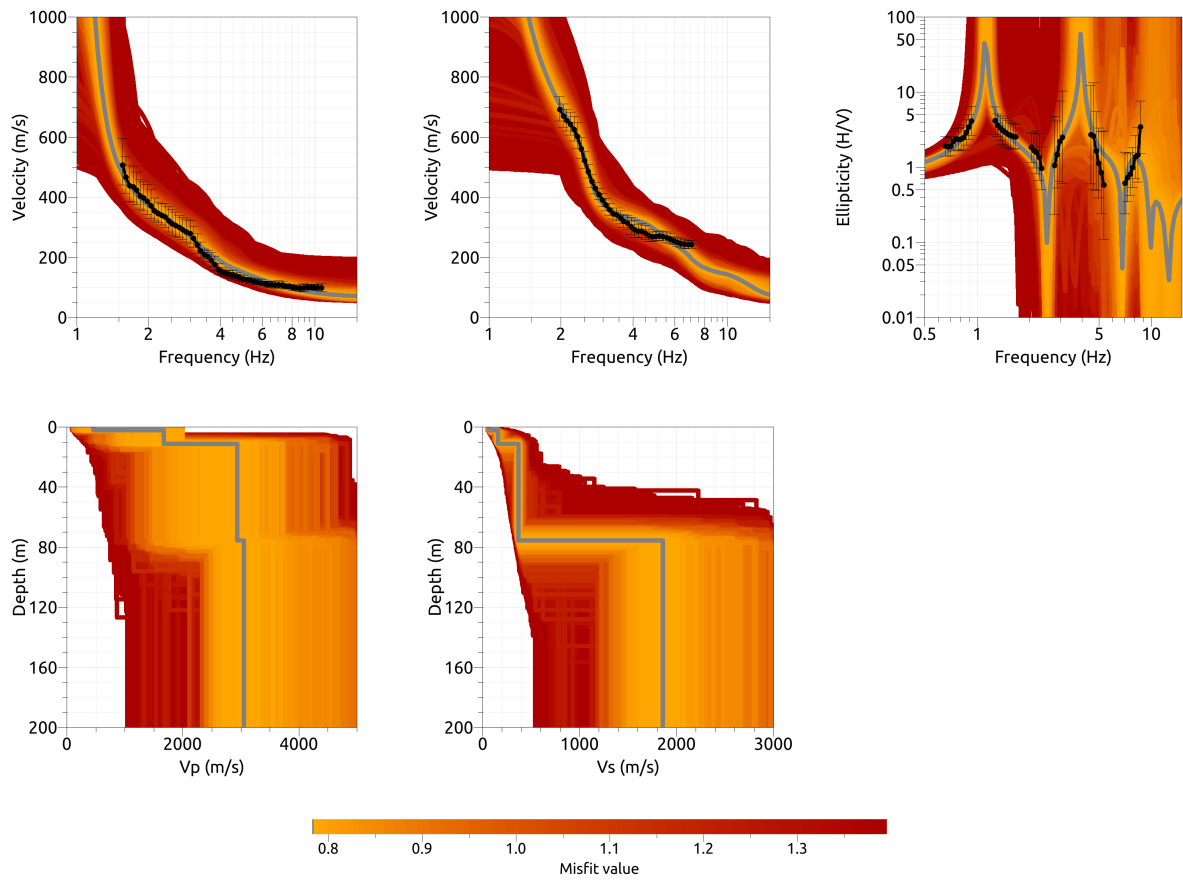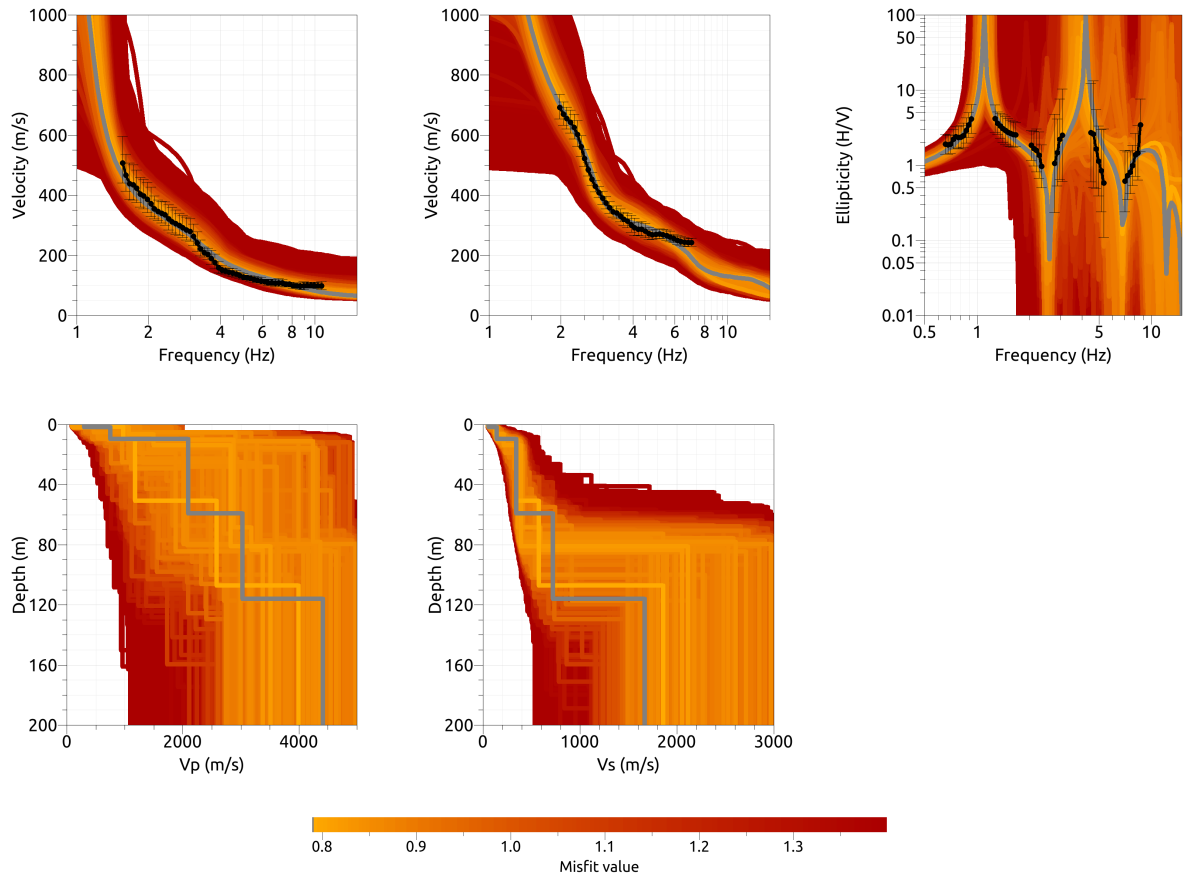
Figure 19: Inversion SBAS04: Love wave fundamental mode dispersion curve (top left), Rayleigh wave fundamental mode dispersion curve (top center), Rayleigh wave ellipticity curve (top right), P-wave velocity profiles (center left) and S-wave velocity profiles (center right). The black dots indicate the data points used for the inversion, the gray line indicates the best-fitting model.

Figure 20: Inversion SBAS05: Love wave fundamental mode dispersion curve (top left), Rayleigh wave fundamental mode dispersion curve (top center), Rayleigh wave ellipticity curve (top right), P-wave velocity profiles (center left) and S-wave velocity profiles (center right). The black dots indicate the data points used for the inversion, the gray line indicates the best-fitting model.
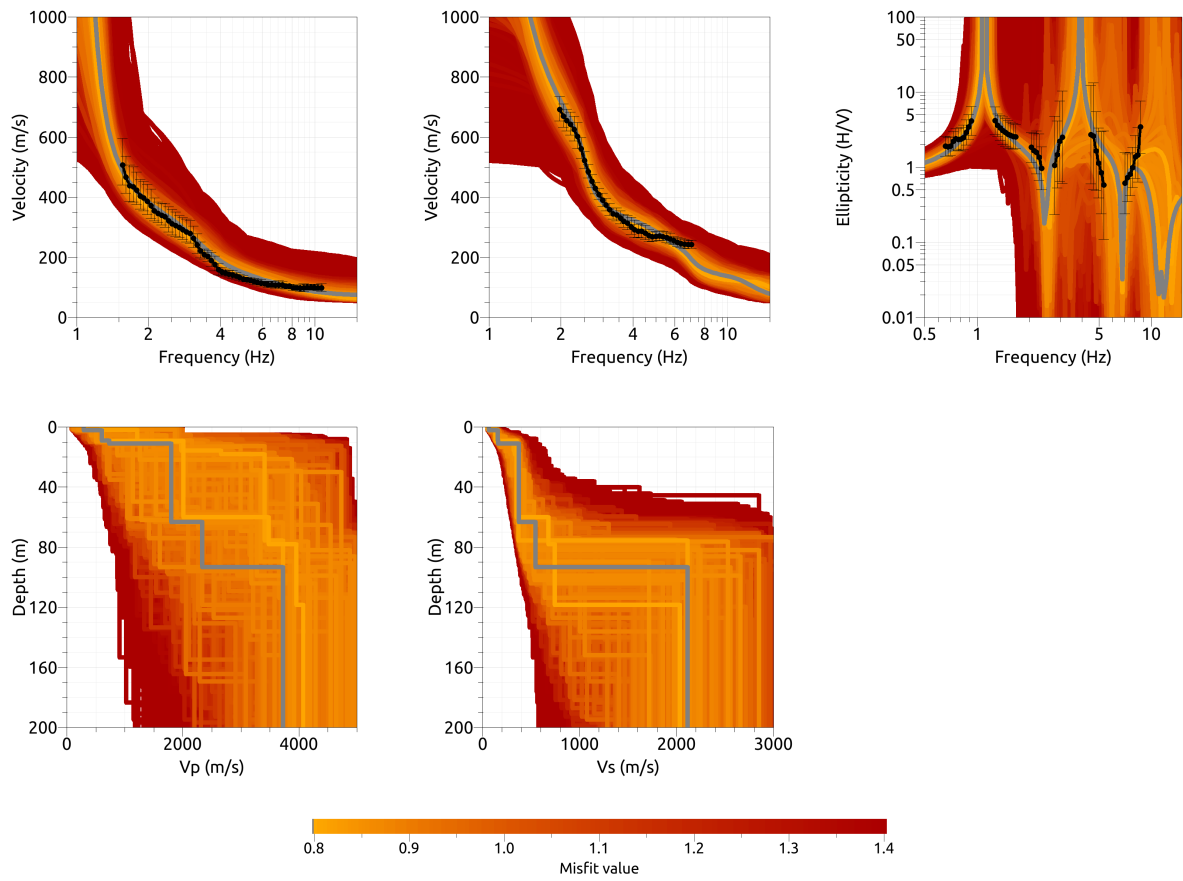
Figure 21: Inversion SBAS06: Love wave fundamental mode dispersion curve (top left), Rayleigh wave fundamental mode dispersion curve (top center), Rayleigh wave ellipticity curve (top right), P-wave velocity profiles (center left) and S-wave velocity profiles (center right). The black dots indicate the data points used for the inversion, the gray line indicates the best-fitting model.
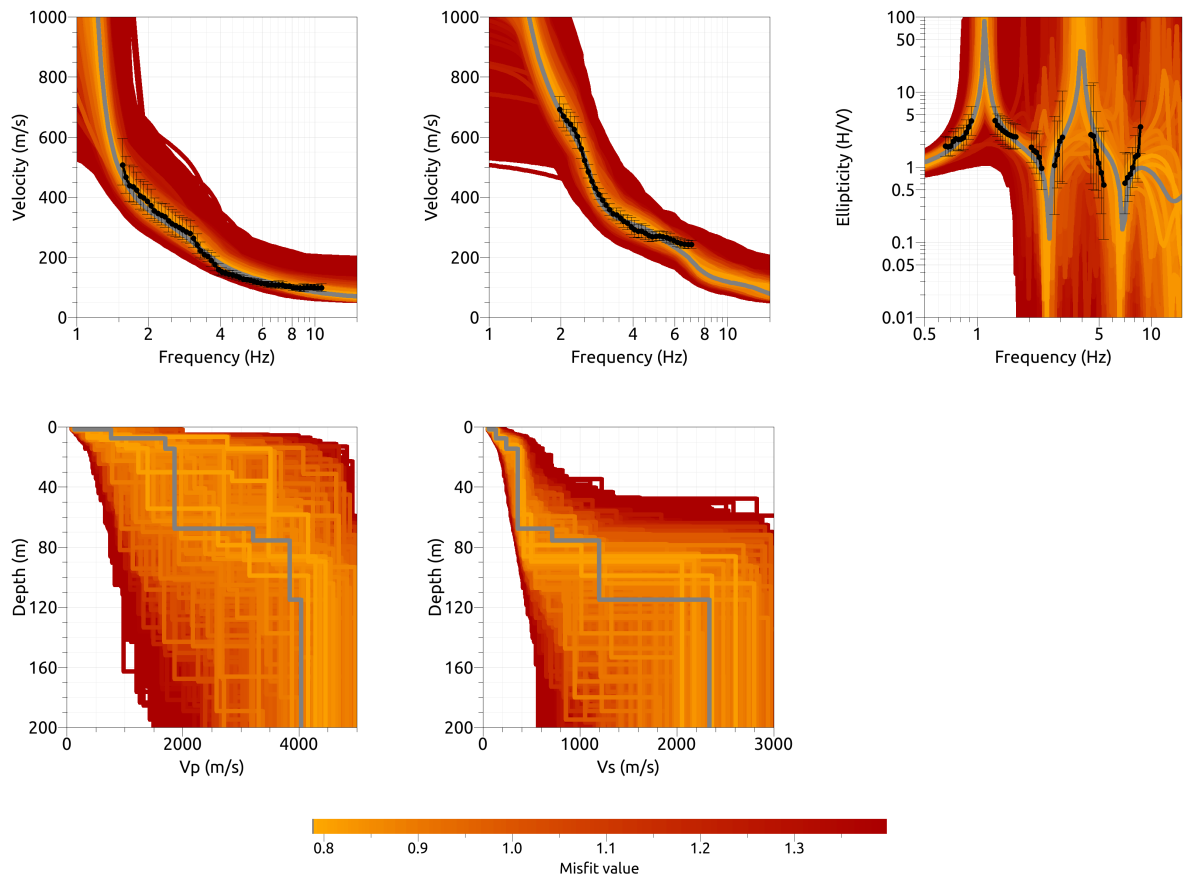
Figure 22: Inversion SBAS07: Love wave fundamental mode dispersion curve (top left), Rayleigh wave fundamental mode dispersion curve (top center), Rayleigh wave ellipticity curve (top right), P-wave velocity profiles (center left) and S-wave velocity profiles (center right). The black dots indicate the data points used for the inversion, the gray line indicates the best-fitting model.
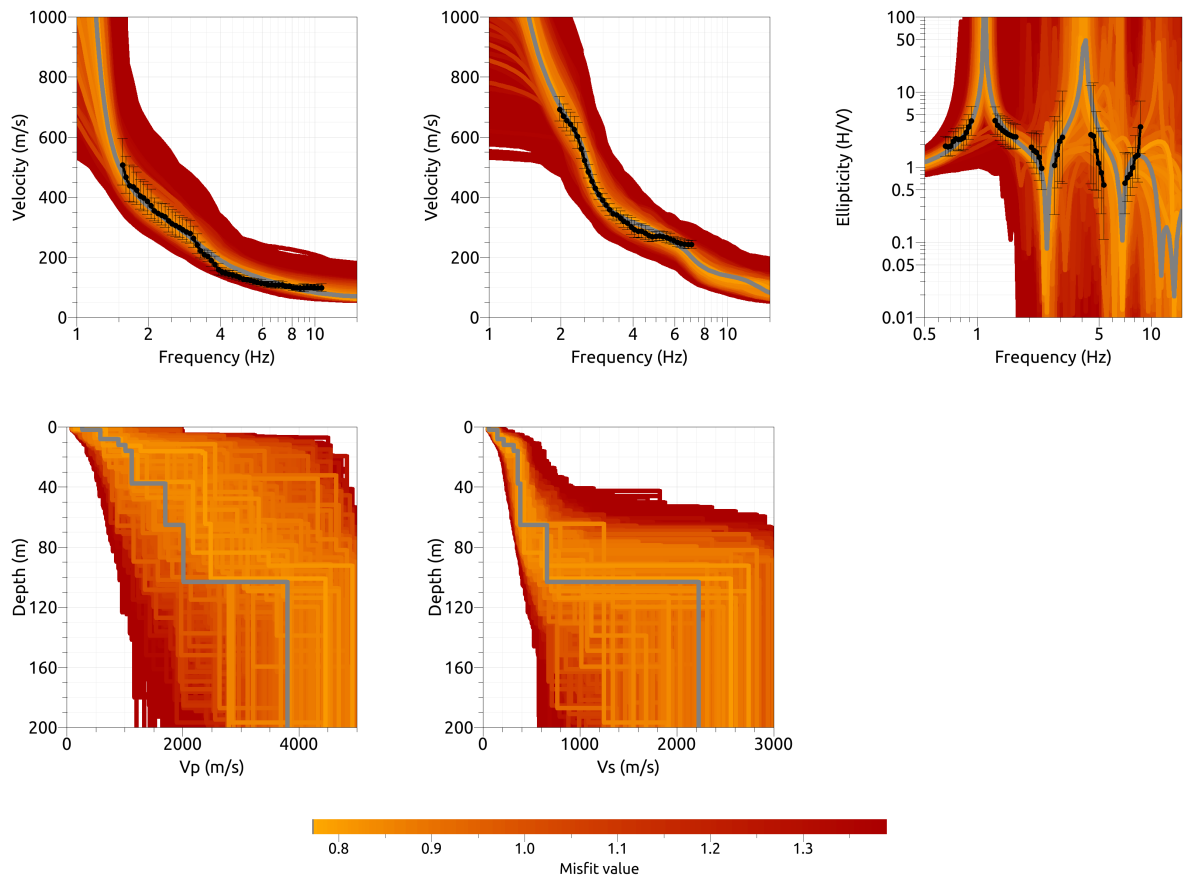
Figure 23: Inversion SBAS08: Love wave fundamental mode dispersion curve (top left), Rayleigh wave fundamental mode dispersion curve (top center), Rayleigh wave ellipticity curve (top right), P-wave velocity profiles (center left) and S-wave velocity profiles (center right). The black dots indicate the data points used for the inversion, the gray line indicates the best-fitting model.
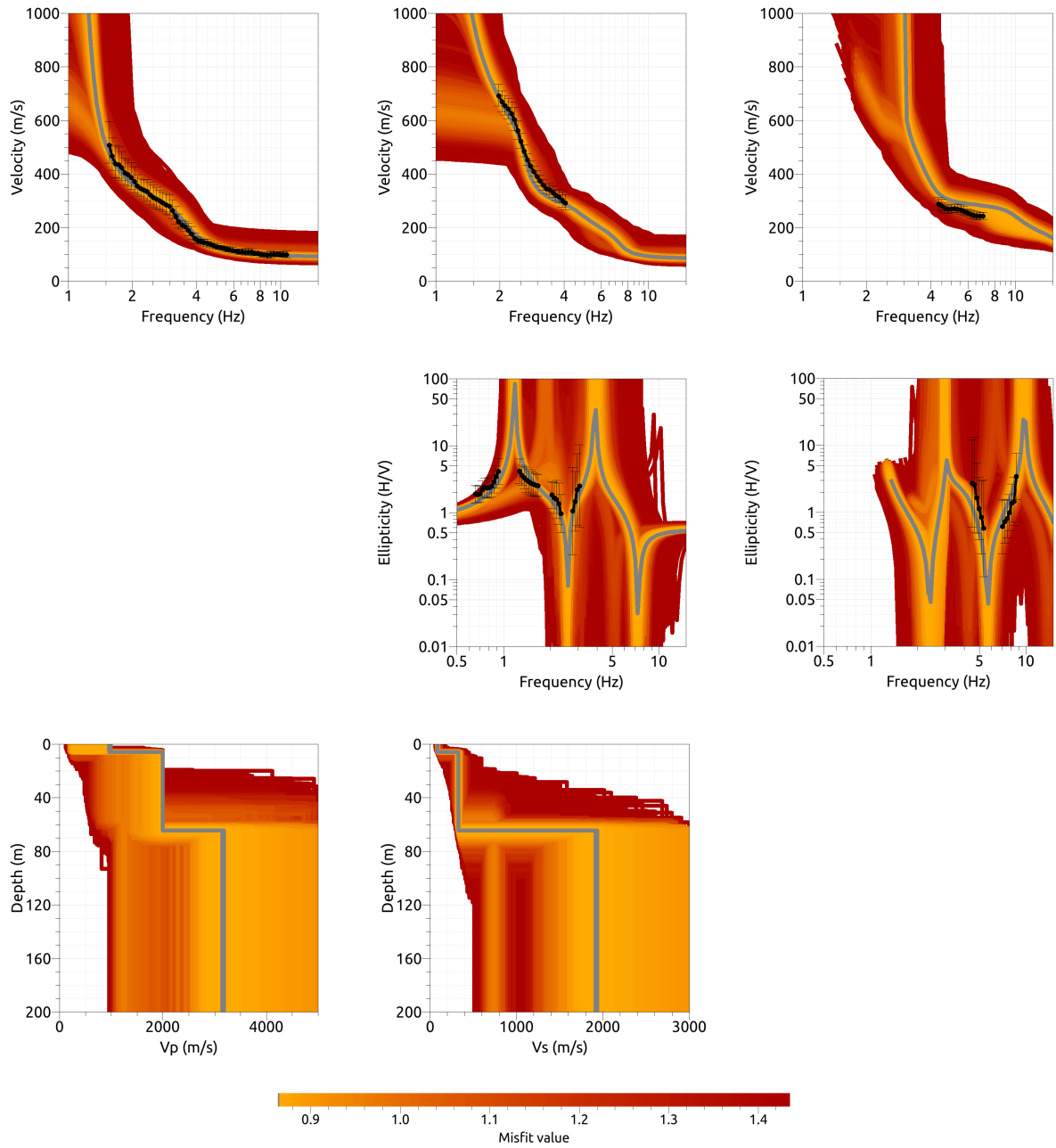
Figure 24: Inversion SBAS03osc: Love wave fundamental mode dispersion curve (top left), Rayleigh wave fundamental mode dispersion curve (top center), Rayleigh wave harmonic mode dispersion curve (top right), Rayleigh wave fundamental mode ellipticity curve (center), Rayleigh wave harmonic mode ellipticity curve (center right), P-wave velocity profiles (bottom left) and S-wave velocity profiles (bottom right). The black dots indicate the data points used for the inversion, the gray line indicates the best-fitting model.
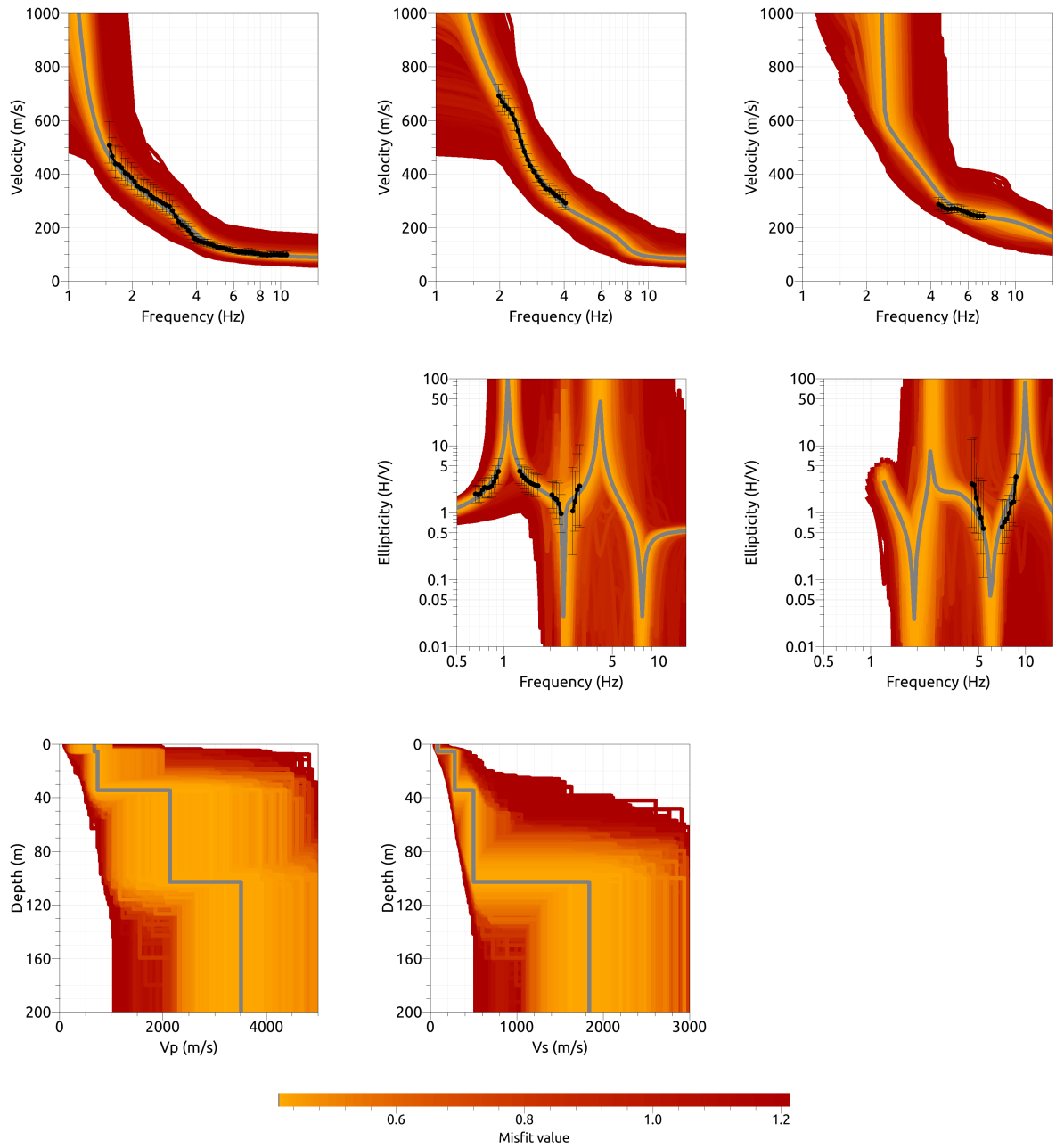
Figure 25: Inversion SBAS04osc: Love wave fundamental mode dispersion curve (top left), Rayleigh wave fundamental mode dispersion curve (top center), Rayleigh wave harmonic mode dispersion curve (top right), Rayleigh wave fundamental mode ellipticity curve (center), Rayleigh wave harmonic mode ellipticity curve (center right), P-wave velocity profiles (bottom left) and S-wave velocity profiles (bottom right). The black dots indicate the data points used for the inversion, the gray line indicates the best-fitting model.
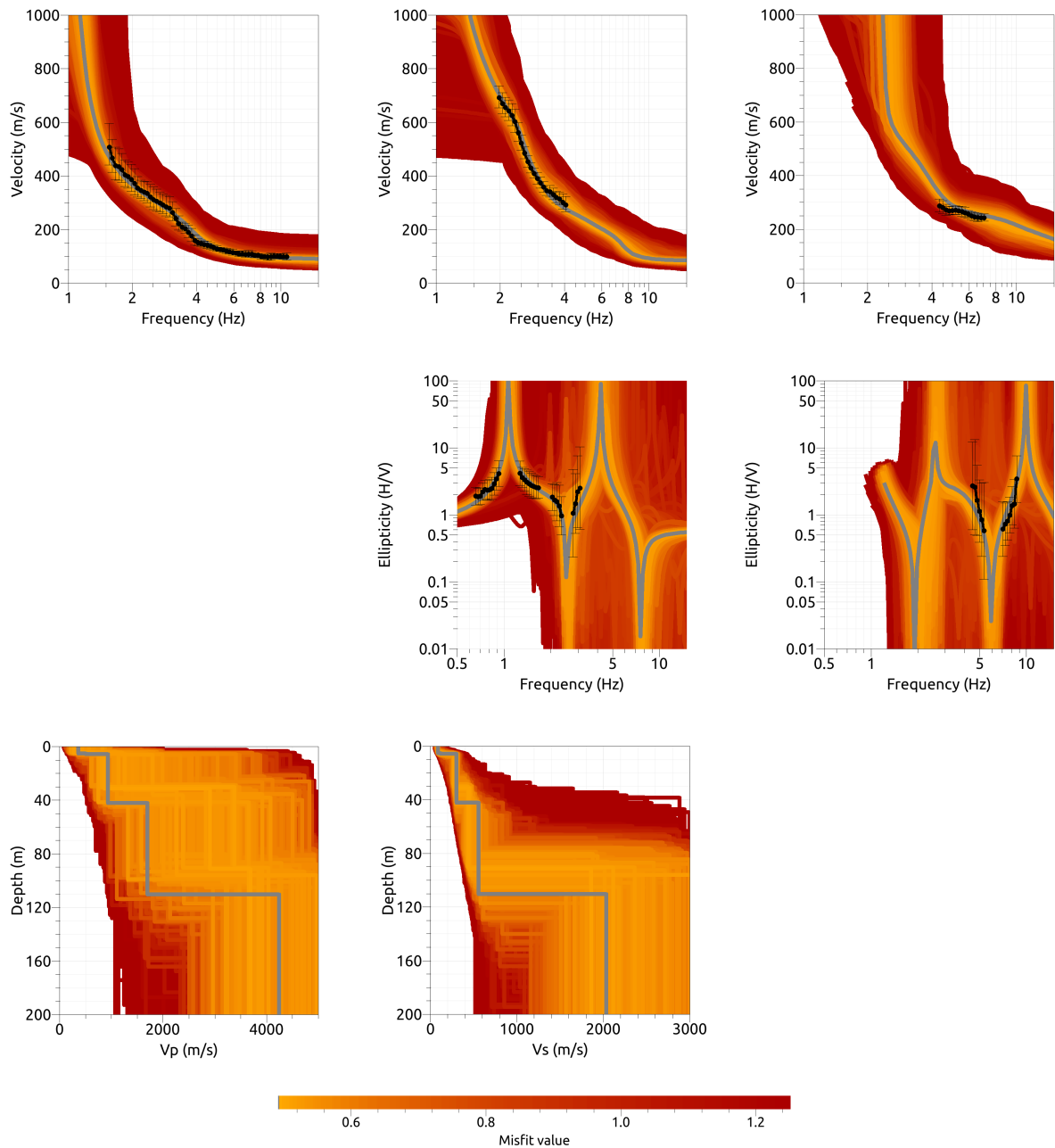
Figure 26: Inversion SBAS05osc: Love wave fundamental mode dispersion curve (top left), Rayleigh wave fundamental mode dispersion curve (top center), Rayleigh wave harmonic mode dispersion curve (top right), Rayleigh wave fundamental mode ellipticity curve (center), Rayleigh wave harmonic mode ellipticity curve (center right), P-wave velocity profiles (bottom left) and S-wave velocity profiles (bottom right). The black dots indicate the data points used for the inversion, the gray line indicates the best-fitting model.

Figure 27: Inversion SBAS06osc: Love wave fundamental mode dispersion curve (top left), Rayleigh wave fundamental mode dispersion curve (top center), Rayleigh wave harmonic mode dispersion curve (top right), Rayleigh wave fundamental mode ellipticity curve (center), Rayleigh wave harmonic mode ellipticity curve (center right), P-wave velocity profiles (bottom left) and S-wave velocity profiles (bottom right). The black dots indicate the data points used for the inversion, the gray line indicates the best-fitting model.
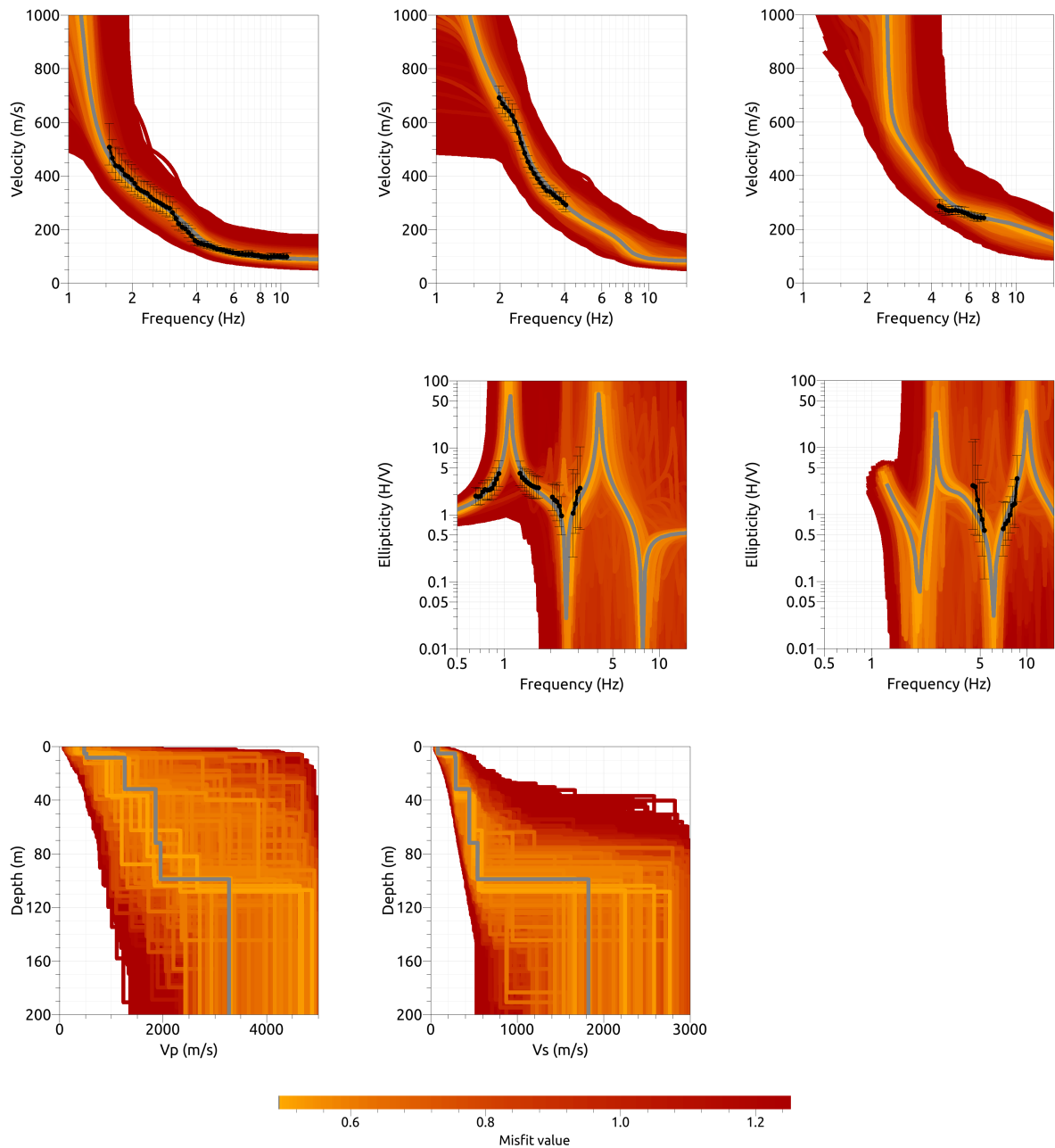
Figure 28: Inversion SBAS07osc: Love wave fundamental mode dispersion curve (top left), Rayleigh wave fundamental mode dispersion curve (top center), Rayleigh wave harmonic mode dispersion curve (top right), Rayleigh wave fundamental mode ellipticity curve (center), Rayleigh wave harmonic mode ellipticity curve (center right), P-wave velocity profiles (bottom left) and S-wave velocity profiles (bottom right). The black dots indicate the data points used for the inversion, the gray line indicates the best-fitting model.
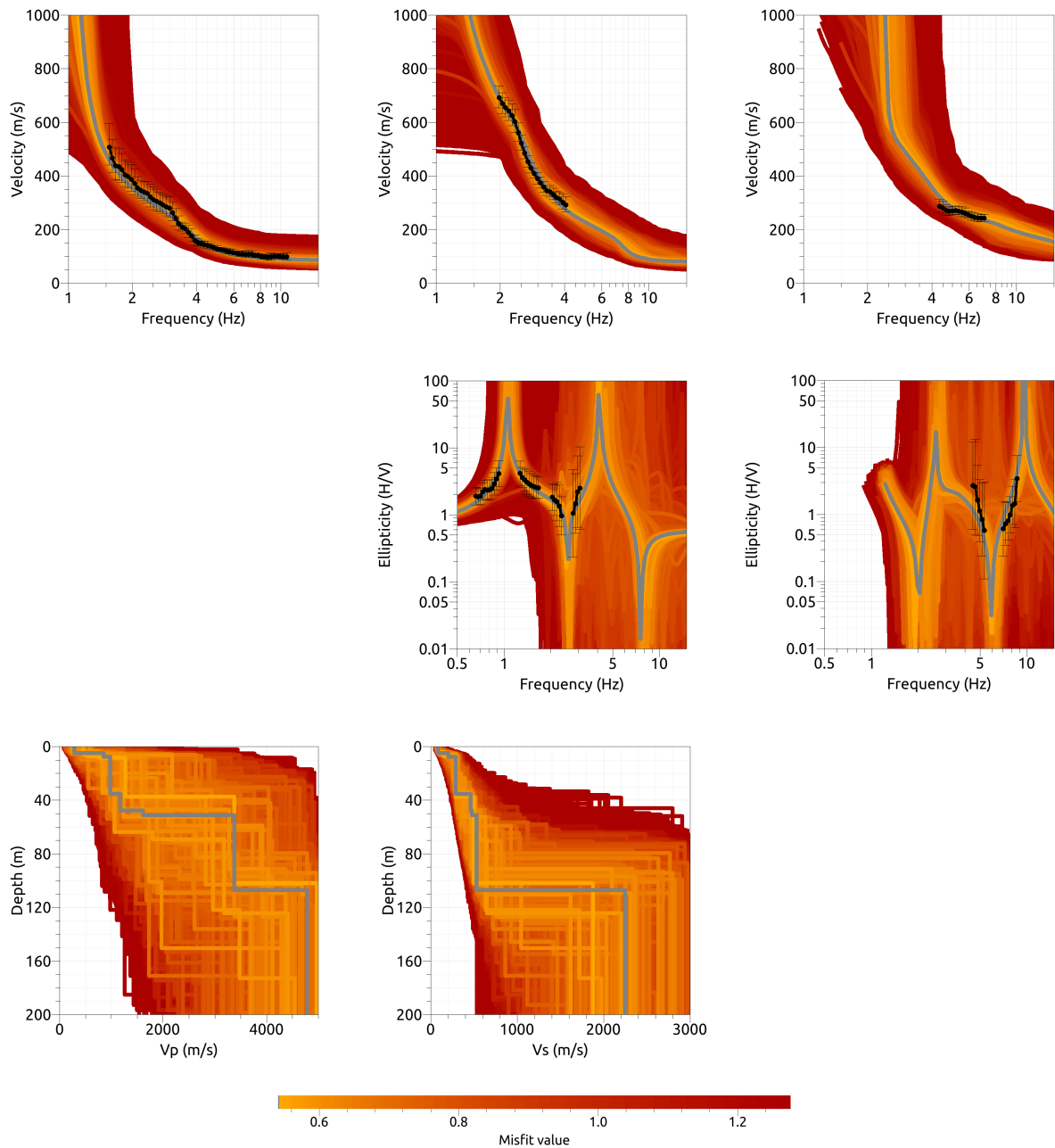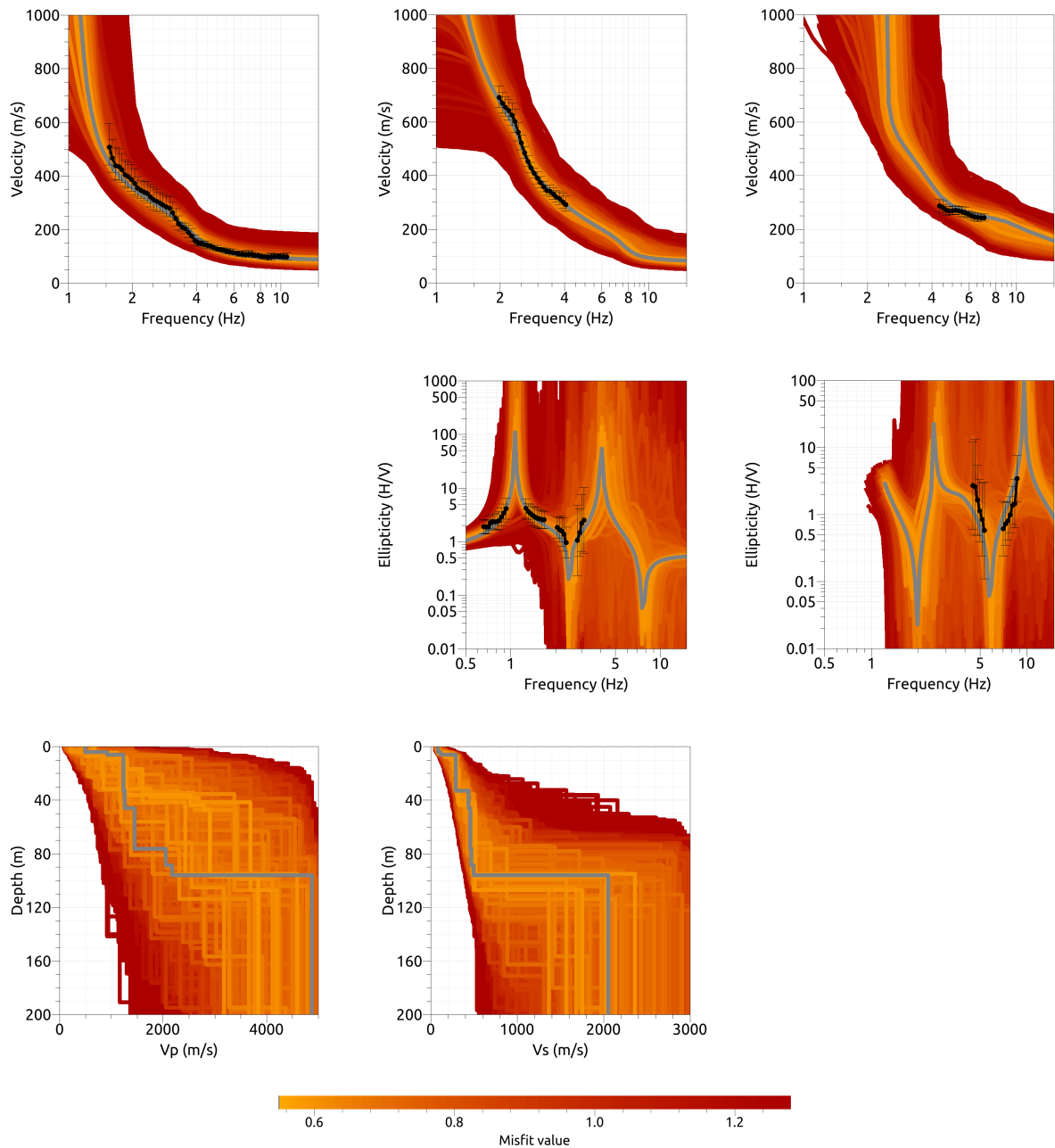
Figure 29: Inversion SBAS08osc: Love wave fundamental mode dispersion curve (top left), Rayleigh wave fundamental mode dispersion curve (top center), Rayleigh wave harmonic mode dispersion curve (top right), Rayleigh wave fundamental mode ellipticity curve (center), Rayleigh wave harmonic mode ellipticity curve (center right), P-wave velocity profiles (bottom left) and S-wave velocity profiles (bottom right). The black dots indicate the data points used for the inversion, the gray line indicates the best-fitting model.

41

5.2.1 Discussion of the inversion result

The best-fitting models of all inversions are shown in Fig. 30. There are some differences between the models without and with osculation. In both cases, the three-layer models differ a lot from all other models and can be disregarded.

The inversions without osculation are all more or less the same in the upper 7 m. The small layer of around 2 m thickness and with a shear-wave velocity of around 60 m/s at the surface corresponds to a theoretical resonance frequency of around 7 to 8 Hz. This is the frequency range of the second trough. Below the small superficial layer, there is a second layer with a shear-wave velocity between 130 and 160 m/s, and another layer with a shear-wave velocity between 340 and 375 m/s. Only the transition between both layers differs significantly between the different parameterizations. For some inversions, the transition consists in a single velocity step, for others, it occurs in two or three steps. The average of all these step depths for the different inversions is around 11 m. Below 60 m, the transition to the bedrock occurs, but it differs a lot between the different inversions. For the four-layer inversion, the transition takes place at 75 m depth, for the seven-layer inversion in several steps with a deepest step at 115 m. In this transition zone, our inversion results are not well constrained. For all models of the inversion with five layers (Fig. 20) and six layers (Fig. 21), the transition zone to the bedrock is badly constrained between 80 and 120 m depth. Also the bedrock velocity is not well constrained, but a value of 2000 m/s seems reasonable.

The inversions with osculation are in a good mutual agreement (except for the 5-layer case) and differ from the models without osculation and can all be well approximated by a four-layer modeling. They show a first layer of around 5 to 6 m thickness with a shear-wave velocity of about 85 m/s. The following layer has an S-wave velocity between 285 and 325 m/s and reaches down to about 34 m, where the third layer with a V_S between 440 and 500 m/s follows. The bedrock is finally reached at a depth of around 100 m (ranging from 96 to 107 m). The bedrock velocity is around 2000 m/s.

The average V_{S30} value of the best-fitting models for the inversions with four to eight layers is $208 \pm 3 \, m/s$ (without osculation) and $203 \pm 3 \, m/s$ (with osculation). The models with osculation are the preferred solutions for this site.
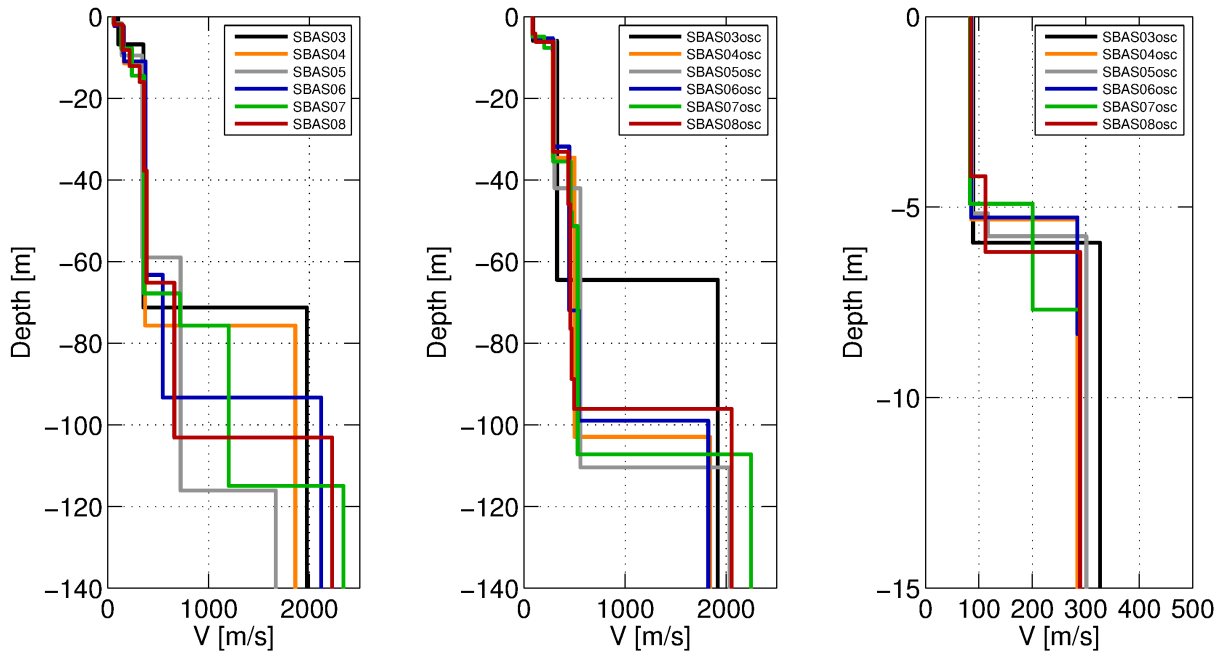
Figure 30: Overview of shear-wave velocity profiles of the best-fitting models of the inversions without osculation (left), as well as for the inversions with osculation in the Rayleigh wave dispersion curve (center) and a zoom on the surface structure for the latter ones (right).

5.3 SH transfer function

The empirical amplification for station SBAS is based on more than ten events so far, the fundamental peak frequency fits very well with the theoretical amplification for the underground models. The higher peak of the transfer function at around 3 Hz also fits with the inverted models. Between both peaks and for higher frequencies, there are major differences between the empirical amplification and the transfer function for the inversion results.
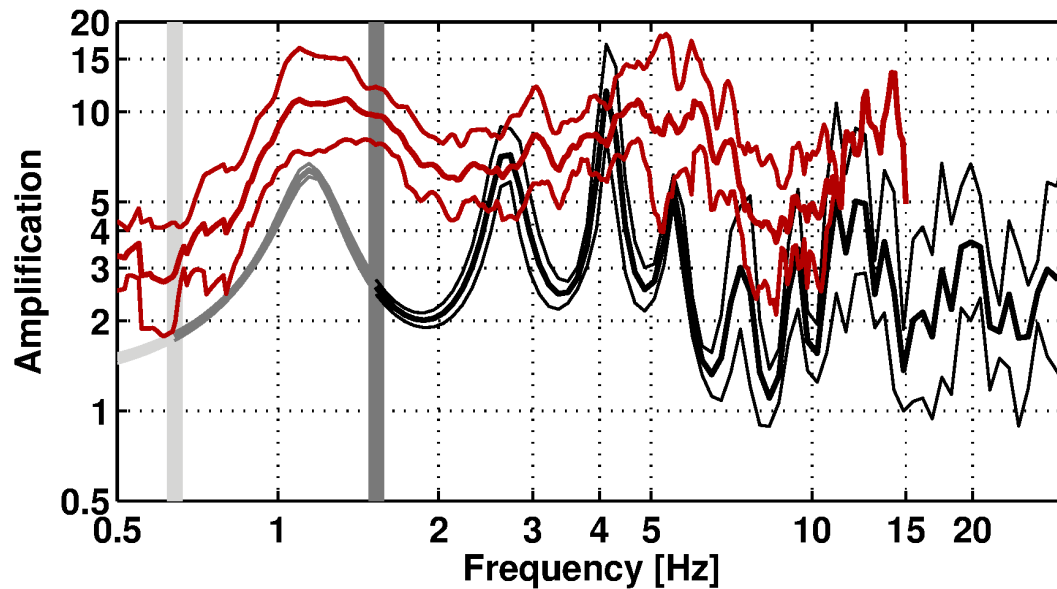

Figure 31: Comparison between the modeled amplification for the best models of the five different inversions with at least four layers and with osculation (black, with standard deviation) and the empirical amplification measured at station SBAS (red, with standard deviation).
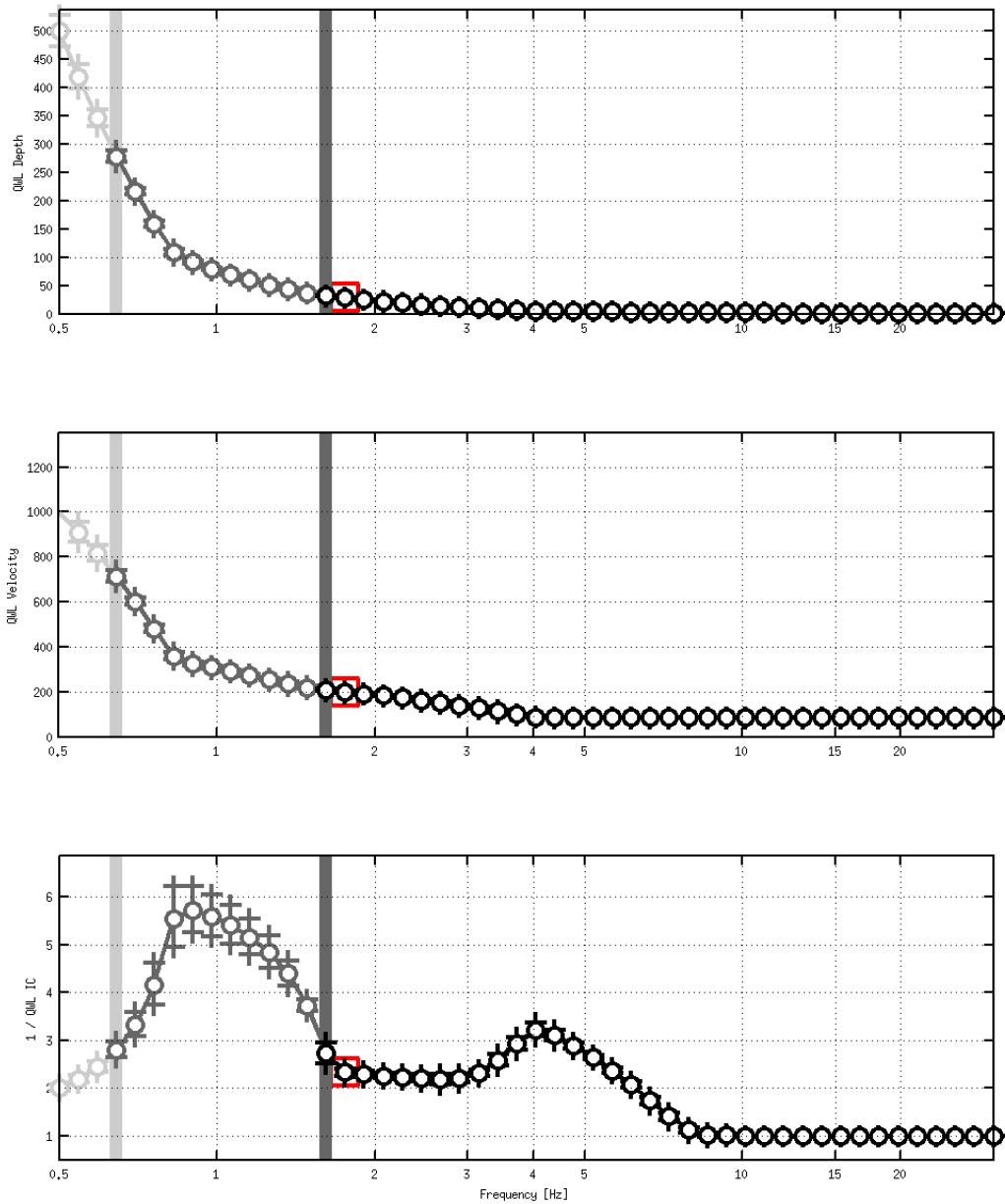
5.4 Quarter-wavelength representation

Figure 32: Quarter wavelength representation of the velocity profile for the best models of the five inversions with at least four layers and with osculation (top: depth, center: velocity, bottom: inverse of the impedance contrast). The black curves are constrained by the dispersion curves, the light grey curves are not constrained by the data. The red square corresponds to V_{S30}.

6 Conclusion

We performed a passive array measurement with two different configurations to characterize the underground under station SBAS in Baar (ZG).

The dispersion curves for both Love and Rayleigh waves could be measured well over a wide frequency range. For Love waves, all measurements match very well. For Rayleigh waves, there are more discrepancies between the different measurements at the lower frequencies. The better inversion results suggest that there is a mode osculation in the measured Rayleigh wave dispersion curve. The ellipticity of the Rayleigh waves was also measured with several techniques. It is rather complicated with two singular peaks and two troughs. RayDec could identify well the fundamental peak as well as the frequencies of the other peak and the troughs, but WaveDec is much stronger in identifying the latter ones in this case. The better inversion results indicate that the first peak and trough of the measurements correspond to the fundamental mode and the higher-frequency part to the first harmonic mode.

The joint inversion of Love and Rayleigh wave dispersion curve and the ellipticity curve showed that a three-layer model can fit such an ellipticity curve, but a good fit is only obtained with at least four layers. The results for models with four to eight layers are similar. The best-fitting models show a first superficial layer of around 6 m thickness with an S-wave velocity of around 85 m/s, followed by a second layer of around 300 m/s down to about 35 m. A third layer of around 470 m/s follows down to a depth of around 100 m, where the bedrock begins. The V_{S30} of the best models is about 203 m/s.

Acknowledgements

References

Aki, K. (1957). Space and time spectra of stationary stochastic waves, with special reference to microtremors. *Bull. Earthquake Res. Inst. Tokyo Univ.*, 35:415–456.

Bettig, B., Bard, P.-Y., Scherbaum, F., Riepl, J., Cotton, F., Cornou, C., and Hatzfeld, D. (2001). Analysis of dense array noise measurements using the modified spatial auto-correlation method (SPAC): application to the Grenoble area. *Boll. Geof. Teor. Appl.*, 42:281–304.

Burjánek, J., Gassner-Stamm, G., Poggi, V., Moore, J. R., and Fäh, D. (2010). Ambient vibration analysis of an unstable mountain slope. *Geophys. J. Int.*, 180:820–828.

Burjánek, J., Moore, J. R., Molina, F. X. Y., and Fäh, D. (2012). Instrumental evidence of normal mode rock slope vibration. *Geophys. J. Int.*, 188:559–569.

Fäh, D., Wathelet, M., Kristekova, M., Havenith, H., Endrun, B., Stamm, G., Poggi, V., Burjanek, J., and Cornou, C. (2009). Using ellipticity information for site characterisation. NERIES deliverable JRA4 D4, available at http://www.neries-eu.org.

Hobiger, M., Bard, P.-Y., Cornou, C., and Le Bihan, N. (2009). Single station determination of Rayleigh wave ellipticity by using the random decrement technique (RayDec). *Geophys. Res. Lett.*, 36.

Maranò, S., Reller, C., Loeliger, H.-A., and Fäh, D. (2012). Seismic waves estimation and wavefield decomposition: Application to ambient vibrations. *Geophys. J. Int.*, 191:175–188.

Poggi, V. and Fäh, D. (2010). Estimating Rayleigh wave particle motion from three-component array analysis of ambient vibrations. *Geophys. J. Int.*, 180:251–267.